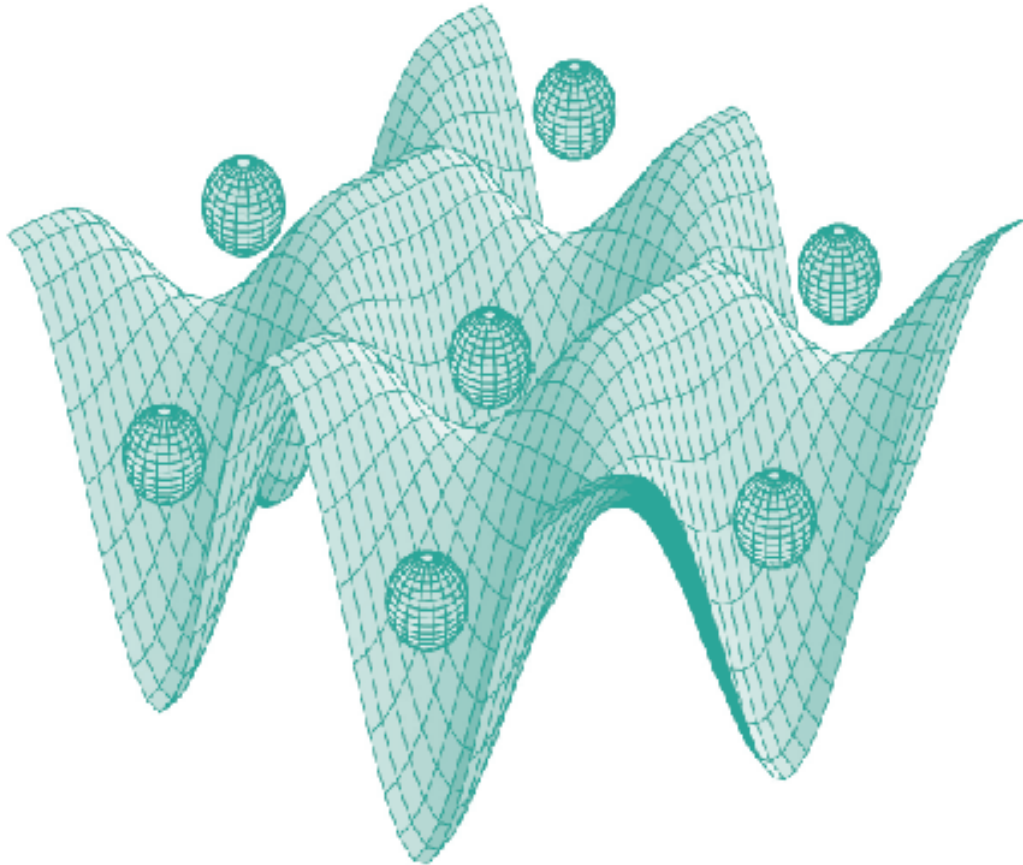




STUDIA UNIVERSITATIS
BABEŞ-BOLYAI



PHYSICA

1-2/2020

**STUDIA
UNIVERSITATIS BABEŞ-BOLYAI
PHYSICA**

1-2/2020
January-December

EDITORIAL OFFICE OF STUDIA UBB PHYSICA:

1, M. Kogălniceanu St., Cluj-Napoca, ROMANIA, Phone: +40 264 405300

http://www.studia.ubbcluj.ro/serii/physica/index_en.html

EDITOR-IN-CHIEF:

Professor Daniel Aurelian ANDREICA, Ph.D., Babeş-Bolyai University, Cluj-Napoca, Romania

EDITORIAL BOARD:

Professor Simion AȘTILEAN, Ph.D., Babeş-Bolyai University, Cluj-Napoca, Romania

Associate Prof. Monica BAIÁ, Ph.D., Babeş-Bolyai University, Cluj-Napoca, Romania

Professor Istvan BALLAI, Ph.D., The University of Sheffield, United Kingdom

Zoltan BALINT, Ph.D., Ludwig Boltzmann Institute Graz, Austria

Professor Titus BEU, Ph.D., Babeş-Bolyai University, Cluj-Napoca, Romania

Prof. Boldizsár JANKÓ, Ph.D., University of Notre Dame, USA

Professor Emil BURZO, Ph.D., Babeş-Bolyai University, Cluj-Napoca, Romania,
member of Romanian Academy

Professor Vasile CHIȘ, Ph.D., Babeş-Bolyai University, Cluj-Napoca, Romania

Professor Olivier ISNARD, Ph.D., University J. Fourier & Institut Neel, Grenoble,
France

Professor Zoltan NEDA, Ph.D., Babeş-Bolyai University, Cluj-Napoca, Romania

Professor Viorel POP, Ph.D., Babeş-Bolyai University, Cluj-Napoca, Romania

Professor Jurgen POPP, Ph.D., Dr.h.c., Institute of Physical Chemistry, Friedrich-Schiller-University Jena, Germany

Professor György SZABÓ, Ph.D., Research Institute for Technical Physics and
Materials Science, Hungarian Academy of Sciences, Budapest, Hungary

Professor Simion SIMON, Ph.D., Babeş-Bolyai University, Cluj-Napoca, Romania

Professor Romulus TETEAN, Ph.D., Babeş-Bolyai University, Cluj-Napoca, Romania

Professor Dietrich ZAHN, Ph.D., Dr.h.c., Technical University, Chemnitz, Germany

Alexis WARTELLE, Ph.D., Neel Institut, Grenoble, France

EXECUTIVE EDITOR:

Lecturer Claudiu LUNG, Ph.D., Babeş-Bolyai University, Cluj-Napoca, Romania

YEAR
MONTH
ISSUE

Volume 65 (LXV) 2020
DECEMBER
1-2

PUBLISHED ONLINE: 2020-12-30
PUBLISHED PRINT: 2020-12-30
ISSUE DOI:10.24193/subbphys.2020

STUDIA UNIVERSITATIS BABEȘ-BOLYAI PHYSICA

1-2

STUDIA UBB EDITORIAL OFFICE: B.P. Hasdeu no. 51, 400371 Cluj-Napoca, Romania,
Phone + 40 264 405352

CUPRINS – CONTENT – SOMMAIRE – INHALT

R. I. CAMPEANU, <i>Positron Impact Ionization of Alkali Atoms</i>	5
R. HIRIAN, P. PALADE, A. CIORÎȚĂ, S. MACAVEI, V. POP, <i>Investigation of Possible Uniaxial Anisotropy in $Co_{11}Zr_2$ Magnetic Phase</i>	11
S. IONITA, K. MAGYARI, A.V. SANDU, V. SIMON, F. IACOMI, <i>Synthesis and Preliminary Characterization of Modified 45S5 Bioglasses</i>	19
SZ. KELEMEN, L. VARGA, Z. NÉDA, <i>Cross-Correlations in the Brownian Motion of Colloidal Nanoparticles</i>	27

V. LORIOT, A. MARCINIAK, S. NANDI, G. KARRAS, M. HERVÉ, E. CONSTANT, E. PLÉSIAT, A. PALACIOS, F. MARTIN, F. LÉPINE, <i>Attosecond Interferometry Using a HHG-2ω_0 Scheme</i>	35
D. M. PETRIȘOR, G. DAMIAN, S. SIMON, <i>EPR Testing of Organic Versus Conventional Musaceae Fruits</i>	49
V. PETROVIĆ, H. DELIBAŠIĆ, I. PETROVIĆ, <i>Tunneling Ionization Study of Linear Molecules in Strong-Field Laser Pulses</i>	57
M. TODICA, <i>P2P (Bilateral) Communication Between NodeMcu ESP8266 Boards Using Arduino IDE</i>	69
C. LUNG, D. MARCONI, M. POP, A.V. POP, <i>Resistance of High-Tc Superconductors: Review Article</i>	87

POSITRON IMPACT IONIZATION OF ALKALI ATOMS

R. I. CAMPEANU^{1,*}

ABSTRACT. The models CPE and CPE4, which were successfully used in positron impact ionization studies, are applied to positron impact ionization of Li, Na and K. This work produces total cross sections which are in agreement with the existing theoretical papers and shows the necessity for experimental measurements of these processes.

Keywords: *Positron collisions; Ionization of Atoms*

1. Introduction

Recent theoretical work on positron impact ionization of atoms and molecules was based on the use of several simple models related to CPE (Coulomb plus plane waves with full energy range). In these models the initial state of the atoms was represented in the Hartree-Fock approximation, while the incident and scattered positron and the ejected electron were described by plane waves and Coulomb waves. We found that a significant improvement in the performance of these distorted wave models was obtained by the inclusion in the final state representation of the electrostatic interaction between the ejected electron and scattered positron. The resulting CPE4 model was shown in [1] to produce good agreement with experiment for hydrogen and all the noble gases. For these targets the model CPE gives results which are not too different from the model CPE4 [2].

For positron impact ionization of alkali atoms there are no experimental data. However for Na and K there are measurements of the total cross sections [3,4], which combined with close coupling calculations of elastic, positronium formation and excitation cross sections [5,6] could in principle suggest the size of the ionization cross sections.

¹ Department of Physics and Astronomy, York University, 4700 Toronto, ON Canada.

* Corresponding author: campeanu@yorku.ca

In this paper we shall use the models CPE and CPE4 for positron impact ionization of alkali atoms. Our cross sections will be compared with other theoretical data available in the literature for lithium [7, 8, 9] and for sodium [10].

2. Theory

Using the partial-wave expansion and performing the angular integrations the electron impact ionization total cross section can be written as:

$$Q(Ei) = \frac{16}{\pi E_i} \int_0^{E/2} dE_e \sum_{l_i l_e l_f} (2L + 1) I(l_i l_e l_f) \quad (1)$$

Here l_i, l_e, l_f represent the orbital angular momentum quantum numbers of the incident, ejected and scattered electrons respectively, E_i is the energy of the incident positron, E_e the energy of the ejected electron, and $E = E_i - I = E_e + E_f$ is the total energy of the scattered positron and ejected electron, where I is the ionization energy. $I(l_i l_e l_f)$ is given by Bransden *et al* [11] as a function of the direct scattering amplitude F :

$$I(l_i l_e l_f) = |F|^2 \quad (2)$$

The CPE model considers that both the ejected electron and scattered positron see the residual atomic ion as a positive single charge:

$$V_i = 0, V_e = -1/r \text{ and } V_f = 0 \text{ for } E_f > E_e \quad (3a)$$

$$V_i = 0, V_e = -2/r \text{ and } V_f = 1/r \text{ for } E_f < E_e \quad (3b)$$

The CPE4 model includes the attraction between the ejected electron and scattered positron:

$$V_e = -\frac{1 - E_e/E_{ef}}{r} \text{ for } E_f > E_e \quad (4)$$

where E_{ef} is given by:
$$E_{ef} = E_e + E_f - 2(E_e E_f)^{1/2} \quad (5)$$

Thus in both models the incident positron is represented as a plane wave, while the ejected electron and scattered positron are represented as Coulomb or plane waves.

Details of the numerical work were presented in a previous paper [12], which dealt with positron impact ionization of He.

3. Results and discussion

Table 1 presents total cross sections for positron impact ionization of the 2s shell of lithium. For the incident energies considered in this paper the contributions from the ionization of the inner shells is insignificant. In addition to our model CPE and CPE4 data we also show the results obtained with models DCPE and EDEC2 by Acacia *et al* [9] and by Mukherjee *et al* [8].

In the paper by Acacia *et al* [9] the model DCPE differs from our model CPE only in the incident channel where it considers the static potential of the target, while their model EDEC2 uses effective charges similarly to our model CPE4. The models used in the distorted wave calculations of Basu *et al* [7] and Mukherjee *et al* [8] are similar to our CPE model. The data of Refs. [7, 8] are available for impact energies equal and lower than 20 eV.

Our CPE data agree with the DCPE data of Ref. [9] and with the data of Refs. [7, 8], while our CPE4 cross sections agree with the EDEC2 data of Ref.[9].

It is interesting to note that for positron impact ionization of Li, Na and K the CPE4 cross sections are significantly larger than the CPE cross sections. This was not the case for other targets such as the noble gases atoms, where the difference was relatively small.

Table 1. Positron-lithium ionization cross sections (in πa_0^2)

E_i (eV)	CPE	CPE4	DCPE	EDEC2	Refs. [7,8]
20	5.63	11.90	5.0	12.5	5.8
30	5.30	9.41	4.2	11.4	
50	3.67	6.13	3.2	7.1	
70	2.40	3.41	2.2	5.2	
100	2.06	2.55	1.6	3.0	

Table 2 presents total cross sections for the positron impact ionization of the 3s shell of sodium. Our data is compared with the distorted wave calculation of Mukherjee *et al* [10], which describes each channel with static and polarization potentials. Our cross sections are significantly larger than those of Ref. [10].

Table 2. Positron - sodium ionization cross sections (in πa_0^2)

E_i (eV)	CPE	CPE4	Ref. [10]
15	8.51	18.14	5.6
20	9.37	19.64	5.4
30	8.16	15.56	4.6
50	5.74	8.29	
70	4.26	5.27	
100	33.05	3.56	

The paper by Hewitt *et al* [6] compares the experimental total cross sections for positron sodium scattering of ref. [3] with the close coupling calculation of elastic + positron formation and excitation cross sections. The agreement is very good but the experimental data are underestimated because in the experiment of ref.[3] it was not possible to discriminate between unscattered positrons and those elastically scattered through small angles in the forward direction. This is why this approach cannot help us to decide the correct size of the positron-Na ionization cross sections.

Table 3 presents total cross sections for the positron impact ionization of the 4s shell of potassium. There are no other theoretical calculations for this process. As for Li and Na the CPE4 data are larger than the CPE data but the shape of the variation with the impact energy is similar.

Table 3. Positron - potassium ionization cross sections (in πa_0^2)

E_i (eV)	CPE	CPE4
10	9.37	22.53
20	10.56	24.36
25	11.12	20.55
30	10.77	16.42
40	9.54	12.17
50	8.07	9.41
70	6.12	6.64
100	4.38	5.08

The paper by Hewitt *et al* [6] does the comparison of experiment and close-coupling theory also for the positron – potassium system. The experimental points in this case are clearly above the theoretical curve particularly at impact energies smaller than 30 eV. Unfortunately from this paper we cannot have the exact suggested ionization cross sections but our data shown in Table 3 agree with the observation of Hewitt *et al* [6] that the ionization cross sections increase significantly at very low impact energies.

4. Conclusions

This work demonstrates that our models CPE and CPE4 produce positron impact ionization cross sections for lithium in agreement with the existing calculations. For all targets the ionization cross sections decrease for increased impact energies, with the CPE4 data being significantly higher than the CPE data.

Our ionization cross sections for sodium are larger than the ionization cross sections of Mukherjee *et al* [10]. For sodium and potassium there are total cross section measurements and by eliminating the theoretical elastic, positronium formation and excitation estimates one could in principle obtain the size of the ionization cross sections. However the existing experimental cross sections are underestimated and therefore this avenue of experimental verification of our data is only partially useful. For potassium this method leads to the observation that the ionization cross sections should increase at energies smaller than 30 eV, which agrees with our findings in Table 3.

Our work shows the necessity for experimental measurements of cross sections for the positron impact ionization of the alkali atoms.

5. Acknowledgement

This research was supported by a grant from the Natural Sciences and Engineering Council of Canada (NSERC).

REFERENCES

1. R.I. Campeanu, R.P. McEachran, A.D. Stauffer, *Can. J. Phys.* **79** (2001) 1231
2. R.I. Campeanu, *Nucl. Instr. and Meth. B* **267** (2009) 239
3. C.K. Kwan, W.E. Kauppila, R.A. Lukaszew, S.P. Parikh, T.S. Stein, Y.J. Wan, M.S. Debabneh, *Phys. Rev. A* **44** (1991) 1620
4. W.E. Kauppila, C.K. Kwan, T.S. Stein, S. Zhou, *J. Phys. B: At. Mol. Opt. Phys* **27** (1994) L551
5. S.J. Ward, M. Horbatsch, R.P. McEachran, A.D. Stauffer, *J. Phys. B: At. Mol. Opt. Phys* **23** (1989) 1845
6. R.N. Hewitt, C.J. Noble, B.H. Bransden, *J. Phys. B: At. Mol. Opt. Phys* **26** (1993) 3661
7. M. Basu, A.S. Ghosh, *J. Phys. B: At. Mol. Opt. Phys* **19** (1986) 1249
8. K.K. Mukherjee, P.S. Mazumdar, *J. Phys. B: At. Mol. Opt. Phys* **21** (1988) 2327
9. P. Acacia, M. Horbatsch, R.P. McEachran, A.D. Stauffer, *J. Phys. B: At. Mol. Opt. Phys* **30** (1997) 2287
10. K.K. Mukherjee, N.R. Singh, K.B. Choudhury, P.S. Mazumdar, *Phys. Rev. A* **46** (1992) 234
11. B.H. Bransden, J.J. Smith, K.H. Winters, *J. Phys. B: At. Mol. Opt. Phys* **12** (1979) 1267
12. R.I. Campeanu, R.P. McEachran, A.D. Stauffer, *J. Phys. B: At. Mol. Opt. Phys* **20** (1987) 1635

INVESTIGATION OF POSSIBLE UNIAXIAL ANISOTROPY IN $\text{Co}_{11}\text{Zr}_2$ MAGNETIC PHASE

R. HIRIAN^{1,2,*}, P. PALADE³, A. CIORÎȚĂ^{4,5}, S. MACAVEI⁵, V. POP¹

ABSTRACT. The $\text{Co}_{11}\text{Zr}_2$ magnetic phase was obtained by a combination of melting, mechanical milling and high temperature annealing. The structure and magnetic properties of the obtained material were investigated. Even though the samples possessed low coercivity, it was shown that they possess uniaxial anisotropy.

Keywords: *hard magnetic materials, magnetic anisotropy, mechanical milling, high temperature annealing*

INTRODUCTION

Permanent magnets are crucially important for modern industry. The high energy product $\text{Nd}_2\text{Fe}_{14}\text{B}$ and highly stable SmCo_5 or $\text{Sm}_2\text{Co}_{17}$ based magnets permit the creation of highly compact devices, such as mobile phones and laptops, while also being excellent at delivering high performance for large applications such as wind turbines and electric vehicles [1-6]. However, the supply of rare-earth elements is tenuous and their extraction and processing has significant environmental impact, therefore a concerted scientific effort has been put forward in recent years towards developing magnetic materials from non-rare earth elements [4]. Amongst the proposed solutions is the $\text{Co}_{11}\text{Zr}_2$ magnetic phase [7], as it has a promising magnetocrystalline anisotropy, excellent temperature stability and good corrosion resistance [8-10], the latter making it suitable for certain specific application where rare-earth based magnets would not fair as well [11].

¹ Faculty of Physics, Babeş-Bolyai University, Cluj-Napoca, RO-400084 Romania

² MedFuture Research Center for Advance Medicine, "Iuliu Hatieganu" University of Medicine and Pharmacy, L. Pasteur 4-6, 400349 Cluj-Napoca, Romania

³ National Institute for Material Physics, P.O. Box MG-7, R-76900 Măgurele, Bucharest, Romania

⁴ Department of Molecular Biology and Biotechnology, Electron Microscopy Laboratory, Biology and Geology Faculty, Babeş-Bolyai University, 5-7 Clinicilor Str., Cluj-Napoca, Cluj County, 400006, Romania

⁵ National Institute for Research and Development of Isotopic and Molecular Technologies, 67-103 Donath Str., Cluj-Napoca, Cluj County, 400293, Romania

* Corresponding author: razvan.hirian@ubbcluj.ro

EXPERIMENTAL

The $\text{Co}_{11}\text{Zr}_2$ alloy was produced by induction melting pure elements under high purity Ar atmosphere. The produced ingot was placed in a tantalum boat and annealed at 1200 °C for 7 days, under high vacuum (10^{-6} mbar), in a Carbolite HVT 12/80/700 furnace, as described in the work used to produce the phase diagram [12]. The produced alloy was then crushed into powder and mechanically milled (MM) for 2 h in a Fritsch Pulverisette 4 planetary ball mill. The milling vials (80 ml) and balls ($\varnothing = 15$ mm) are made of 440C hardened steel. The ratio between the rotation speed of the disk and the absolute rotation of the vials was $\Omega/\omega = 333$ rpm/- 566 rpm with a ball to powder weight ratio of 10:1. The milled powder was then re-annealed at 1200 °C in the same conditions as the bulk ingot.

Crystalline structure of the produced material was investigated using X-ray diffraction, on a Bruker D8 Advance diffractometer equipped with a Cu source. The structure was refined using the Fullprof software, with only space group and unit cell parameters, as the atomic positions are still debated in the literature. The microstructure of the sample was investigated by scanning electron microscopy (SEM), on a Hitachi SU8230, while the soichimotery of the samples was checked by Energy Dispersive X-Ray Spectroscopy (EDX) on the same device.

For magnetic measurements the powders were blocked in epoxy and left to set in a homogenous applied magnetic field of 0.2 T until fully hardened. Thus two samples were produced, one with grains aligned along and one perpendicular to the applied field direction. An isotropic sample, left to harden in zero field, was also produced for reference.

The magnetic measurements were carried out using a vibrating sample magnetometer in a temperature range of 6 K to 300 K and in applied fields of up to 6 T.

First order reversal curves (FORC) were measured on the isotropic sample, at room temperature with a reversal (H_{rev}) and applied field (H_{app}) step of 0.01 T, from -0.5 to 0.5 T as the hysteresis loop fully closes at these fields. For the calculation of the FORC the program DoFORC [13] was used.

The FORC distribution is defined as the mixed second derivative of the first order reversal curves:

$$\rho_{FORC} = -\frac{1}{2} \frac{\partial^2 m_{FORC}(H_{rev}, H_{app})}{\partial H_{rev} \partial H_{app}} \quad (1)$$

where m is the magnetization.

The temperature dependence of the anisotropy constants was determined by the Sucksmith-Thompson method [14]:

$$\frac{\mu_0 H_{app}}{M_{\perp}} = \frac{2K_1}{M_s^2} + \frac{4K_2}{M_s^4} M_{\perp}^2 + N_D \quad (2)$$

where μ_0 is the magnetic permeability of vacuum H_{app} is the applied magnetic field, M_{\perp} is the magnetization for the perpendicular aligned sample, K_1 and K_2 are the first and second anisotropy constants, M_s is the saturation magnetization and N_D is the demagnetization factor, measured as the slope (in the magnetization curve) at low field for the parallel oriented sample.

RESULTS AND DISCUSSION

The structure of the $\text{Co}_{11}\text{Zr}_2$ sample was refined using the orthorhombic structure, space group Pcna . The results of the fitting as shown in **Fig. 1**, the obtained lattice parameters were $a=4.83(2)$ Å, $b=8.178(6)$ Å and $c=32.9(2)$ Å, values in agreement with the current state of the art, cited in the literature [9].

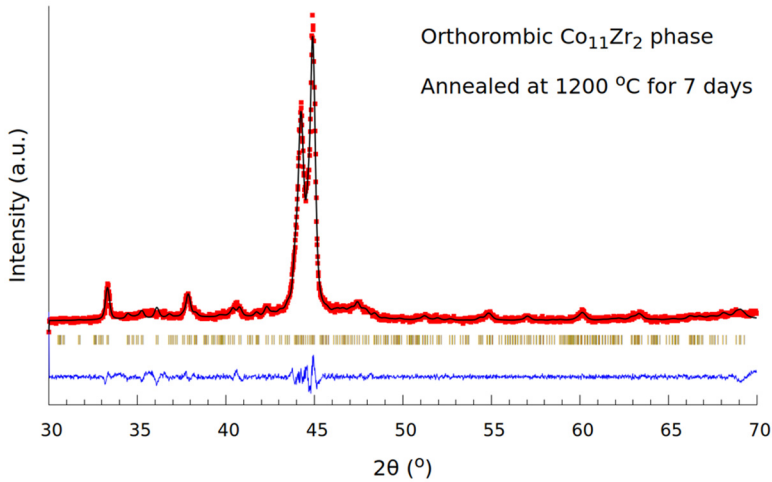


Fig. 1. Rietveld refinement for $\text{Co}_{11}\text{Zr}_2$ annealed at 1200 °C for 7 days, with orthorhombic structure. XRD pattern red point, fit black line, reflection position olive bar. The difference between the XRD pattern and calculated structure is given as the blue line (below)

The fit in **Fig. 1** was made using only the structure factor for the $\text{Co}_{11}\text{Zr}_2$ orthorhombic phase, as the atomic positions are not yet known in the literature. Therefore the large peak around 45 deg could be convoluted with Co. As such, the refinement was repeated with the addition of the Co phase, and the maximum possible Co content was determined to be 3%, an amount comparable to the error of determination. However, the XRD analysis is good enough to exclude the $\text{Co}_{23}\text{Zr}_6$ and $\text{Co}_{11}\text{Zr}_2$ romboedral [15] phases.

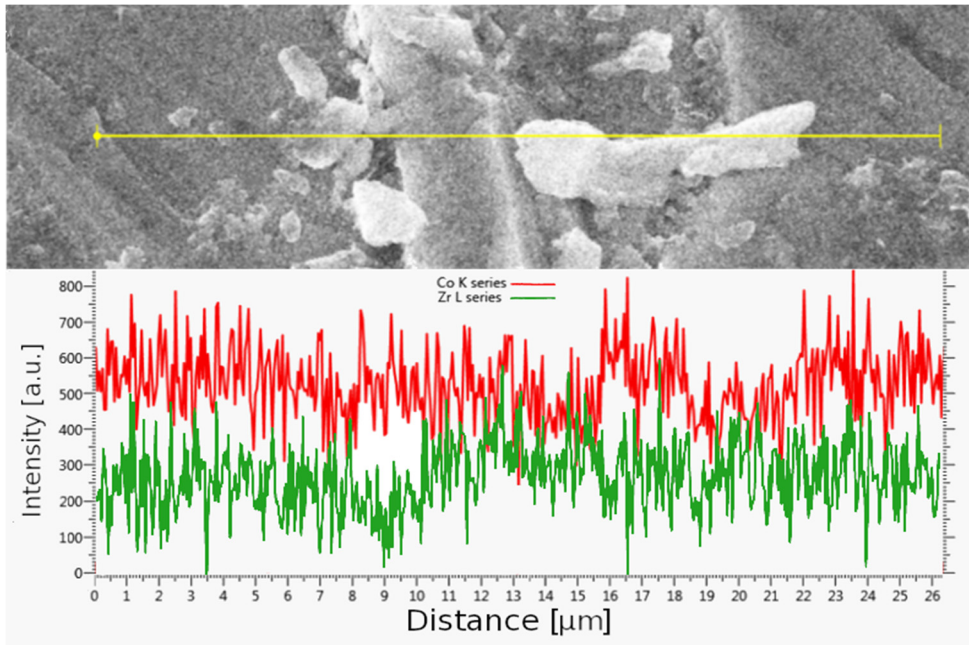


Figure 2. SEM image and corresponding EDX line scan data (for Co and Zr) of investigated region

The EDX analysis showed that the stoichiometry of the material is that of the $\text{Co}_{11}\text{Zr}_2$ phase, while line scans, selected image shown in

Figure 2, prove that the ratio between the two constituent elements does not vary significantly through the material.

First order reversal curves, measured at 300 K, show that the isotropic sample is a rather soft magnetic material. Most reversal processes take place very close to the reversible axis. The maximum reversal is centered around 0 T, the samples themselves showing a coercive field at 300 K of just 0.01 T.

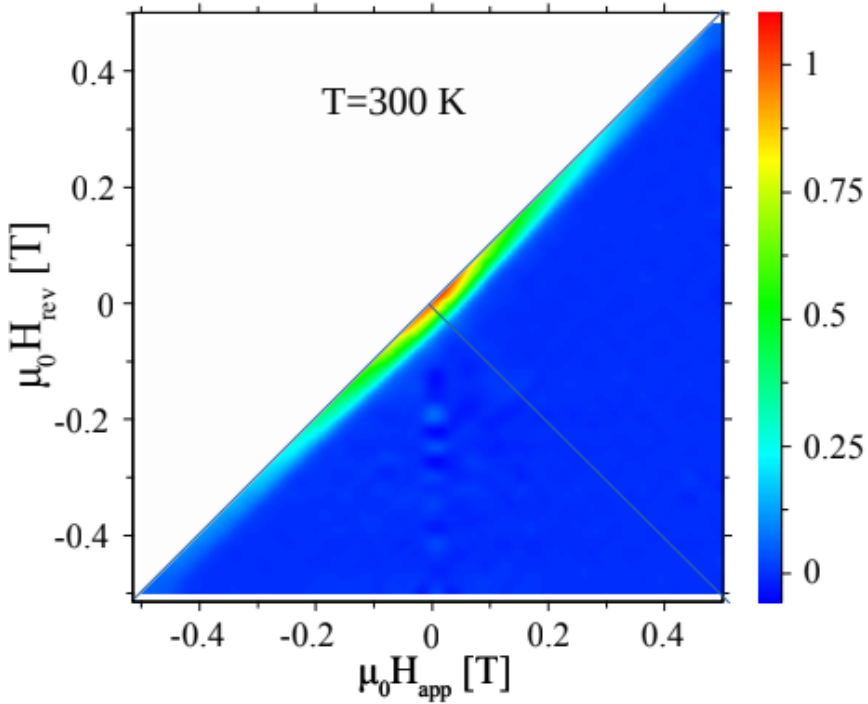


Figure 3. FORC distribution for $\text{Co}_{11}\text{Zr}_2$ alloy recorded at room temperature

Magnetization measurements were also carried out on the aligned samples, between 6 K and 300 K,

Figure 4a. These measurements indicate that although the samples are not fully aligned, the curves are not straight lines, there are significant and systematic differences between the magnetization curves of the parallel and perpendicular aligned samples, from low temperature to room temperature. Therefore, using the Sucksmith-Tompson method, the anisotropy constants were determined, shown in

Figure 4b. While the values of both parameters are low (very likely due to the significant misalignment present in the samples) both anisotropy constants are positive which is a strong indicator of uniaxial anisotropy.

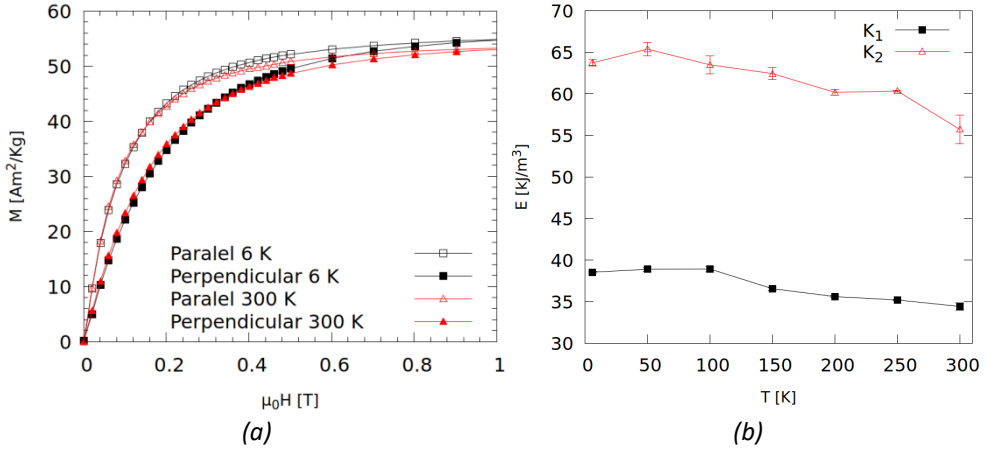


Figure 4. Magnetization measurements on aligned (parallel and perpendicular) $\text{Co}_{11}\text{Zr}_2$ samples (a) and anisotropy constants as a function of temperature (b).

CONCLUSIONS

The $\text{Co}_{11}\text{Zr}_2$ magnetic phase was successfully obtained by a combination of induction melting mechanical milling and high temperature annealing. The magnetic properties of the alloy were investigated and the evolution of the magnetocrystalline anisotropy was studied in a temperature range between 6 and 300 K. The value of the uniaxial anisotropy energy for the magnetic phase was found to be very stable up to room temperature, the total anisotropy energy dropping by only 15% between 6 and 300 K.

ACKNOWLEDGMENTS

We would like to acknowledge the financial support of the Romanian Ministry of Research and Innovation, grant PN-III-P1-1.2-PCCDI-2017-0871.

REFERENCES

1. D. Sander, S. O. Valenzuela, D. Makarov, C. H. Marrows, E. E. Fullerton, P. Fischer, J. McCord, P. Vavassori, S. Mangin, P. Pirro, et al. *J. Phys. D. Appl. Phys.* 50 (2017), doi:10.1088/1361-6463/aa81a1
2. J. M. D. Coey, *IEEE Trans. Magn.* 47, 4671-4681, (2011) doi:10.1109/TMAG.2011.2166975
3. D. Goll, H. Kronmüller, *Naturwissenschaften* 87, 423-438, (2000), doi:10.1007/s001140050755
4. J. M. D. Coey, *Engineering* 6, 119–131, (2020) doi:10.1016/j.eng.2018.11.034
5. N.T. Nassar, X. Du, T.E. Graedel, *J. Ind. Ecol.* 19, 1044–1054, (2015) doi:10.1111/jiec.12237
6. K. Binnemans, P.T. Jones, B. Blanpain, T. Van Gerven, Y. Yang, A. Walton, M. Buchert, *J. Clean. Prod.* 51, 1–22, (2013) doi:10.1016/j.jclepro.2012.12.037
7. T. Ishikawa, K. Ohmori, *IEEE Trans. Magn.* 26, 1370-1372, doi: <https://doi.org/10.1109/20.104381>
8. X. Zhou, J. Zhang, X. Liao, J. He, K. Li, Z. Liu J. Magn. Mater. 501, 166483, (2020) doi: <https://doi.org/10.1016/j.jmmm.2020.166483>
9. Z. Li, W.Y. Zhang, D.J. Sellmyer, X. Zhao, M.C. Nguyen, C.Z. Wang, K.M. Ho, *J. Alloy. Compd.*, 611, 167-170, (2014) doi: <https://doi.org/10.1016/j.jallcom.2014.05.072>
10. S. Manjura Hoque, S.K. Makineni, A. Pal, P. Ayyub, K. Chattopadhyay, *J. Alloy. Compd.*, 620, 442-450, (2015), doi: <http://dx.doi.org/10.1016/j.jallcom.2014.09.104>
11. Y. Ouyang, R. Qiu, Y. Xiao, Z. Shi, S. Hu, Y. Zhang, M. Chen, P. Wang, *Chem. Eng. J.* 368, 331-339, (2019), doi: <https://doi.org/10.1016/j.cej.2019.02.126>
12. X.J. Liu, H.H. Zhang, C.P. Wang, K. Ishida, *J. Alloy. Compound*, 482, 99-105, (2009), doi:10.1016/j.jallcom.2009.04.032
13. D. Cimpoesu, I. Dumitru, A. Stancu, *J Appl Phys*, 125, 023906 (2019), doi: 10.1063/1.5066445
14. W. Sucksmith, J.E. Thompson, *Proc. R. Soc. London, Ser. A* 225, 362, (1954)
15. X. Zhao, L. Ke, M. C. Nguyen, C-Z. Wang, K-M. H, *J. Appl. Phys.* 177, 243902 (2015), doi: <http://dx.doi.org/10.1063/1.4922984>

SYNTHESIS AND PRELIMINARY CHARACTERIZATION OF MODIFIED 45S5 BIOGLASSES

S. IONITA¹, K. MAGYARI², A.V. SANDU³, V. SIMON⁴, F. IACOMI^{1,*}

ABSTRACT. The study is devoted to synthesis and preliminary structural and morphological characterization of modified 45S5 glasses, in $(66-x)\text{SiO}_2\cdot 27\text{CaO}\cdot 4\text{P}_2\text{O}_5\cdot 3\text{TiO}_2\cdot x\text{Al}_2\text{O}_3$ system, with potential applications in dentistry. The composition of the sol-gel derived samples was verified with respect to their nominal composition. The effect of partial SiO_2 replacement with Al_2O_3 on samples structure and morphology is investigated. It was established that the Ca/P ratio is diminished in Al_2O_3 containing samples and that an amorphous hydroxyapatite phase similar to hydroxyapatite reported for bone tissue is formed.

Keywords: *bioglasses; sol-gel-synthesis; XRD; SEM; EDX.*

INTRODUCTION

Bioactive glasses and oxide glass components introduced into composite materials represent an important class in biomaterials field with applications in orthopaedics and dentistry [1,2]. When in contact with the body fluid, these materials generate a series of chemical and physical reactions that lead to the formation of hydroxyapatite – the mineral phase of bone tissue. Bone and enamel share the same hydroxyapatite mineral phase, but they differ in morphology and organic content. The composition of enamel is nearly completely inorganic, while bone has a relatively high organic composition. In pure hydroxyapatite, $\text{Ca}_5(\text{PO}_4)_3(\text{OH})$ - often noted $\text{Ca}_{10}(\text{PO}_4)_6(\text{OH})_2$, the ratio between the number of calcium and phosphorus atoms is $\text{Ca}/\text{P} = 1.67$, while in different bone tissues it differs and takes values encompassed in $1.9 < \text{Ca}/\text{P} < 2.2$ range and even outside of that [3,4].

¹ Faculty of Physics, Alexandru Ioan Cuza University, Iasi, Romania

² Interdisciplinary Research Institute on Bio-Nano-Sciences, Babes-Bolyai University, Cluj-Napoca, Romania

³ Faculty of Materials Science and Engineering, Gheorghe Asachi Technical University, Iasi, Romania

⁴ Faculty of Physics & Interdisciplinary Research Institute on Bio-Nano-Sciences, Babes-Bolyai University, 400084 Cluj-Napoca, Romania

* Corresponding author: iacomi@uaic.ro

Oxide glasses of $\text{SiO}_2\text{-CaO-P}_2\text{O}_5$ system are a class of materials with high potential for applications such as bioactive glasses for bone tissue repair, tissue regeneration and other various dental applications [5-10].

An important characteristic of composite materials containing bioactive glass is the proportion of the glass phase which influences the mechanical properties. The elimination of residual stresses and cracks at the microscopic level play a key role in the development of high-strength biomaterials. The term "bioglass" was initially introduced for the glass with the composition 46.1 mol.% SiO_2 , 24.4 mol.% Na_2O , 26.9 mol.% CaO and 2.6 mol.% P_2O_5 , registered as Bioglass[®], with consecrated denomination as 45S5 bioglass [11]. The partial replacement of Na_2O and CaO with other oxides may improve certain glass properties. For example, the replacement with K_2O and MgO allows the control of expansion coefficient [12,13].

The compositional range of 45S5 bioglass can be enlarged by introducing oxides like TiO_2 and Al_2O_3 , which may increase the activation energy of crystallization [14]. Moreover, it was reported that the addition of TiO_2 and Al_2O_3 improves the mechanical properties of glasses and enhances their adherence to bone tissue [15,16].

The aim of this paper was the synthesis and preliminary structural and morphological characterization of modified 45S5 glasses, in $(66-x)\text{SiO}_2\cdot 27\text{CaO}\cdot 4\text{P}_2\text{O}_5\cdot 3\text{TiO}_2\cdot x\text{Al}_2\text{O}_3$ system. At the same time, the composition of the prepared samples was verified with respect to their nominal synthesis composition. The structural and morphological effect of the new glass system as well as the partial SiO_2 replacement with Al_2O_3 is considered of interest for the design of composite biomaterials with potential applications in dentistry.

EXPERIMENTAL

Glasses of $(66-x)\text{SiO}_2\cdot 27\text{CaO}\cdot 4\text{P}_2\text{O}_5\cdot 3\text{TiO}_2\cdot x\text{Al}_2\text{O}_3$ system, with $x= 0, 1$ and 2 mol% (Table 1), were prepared by sol-gel method, which is largely applied to obtain bioactive glasses [5,6,15,16]. Tetraethyl orthosilicate ($\text{Si}(\text{OC}_2\text{H}_5)_4$ – TEOS), triethyl phosphate ($(\text{C}_2\text{H}_5)_3\text{PO}_4$ - TEP), calcium nitrate tetrahydrate ($\text{Ca}(\text{NO}_3)_2\cdot 4\text{H}_2\text{O}$), titanium isopropoxide ($(\text{Ti}[\text{OCH}(\text{CH}_3)_2]_4$ - TIP) and aluminum nitrate nonahydrate ($\text{Al}(\text{NO}_3)_3\cdot 9\text{H}_2\text{O}$) were used as precursors of the component oxides. For hydrolysis with HNO_3 , the molar ratio $(\text{HNO}_3 + \text{H}_2\text{O}) / (\text{TEOS} + \text{TEP})$ was kept 8.

The gelation was achieved after 24 hours by maintaining the solution at 37°C . Then the gels were aged at 37°C for 3 days, and thereafter they were dried at 110°C for 24 hours. Finally, a heat treatment at 600°C was applied for 3 hours, to eliminate the synthesis residues and to obtain a stabilized structure.

Table 1. Notation and nominal composition of the investigated samples

Notation	Composition (mol %)
P ₀	66SiO ₂ ·27CaO·4P ₂ O ₅ ·3TiO ₂
P ₁	65SiO ₂ ·27CaO·4P ₂ O ₅ ·3TiO ₂ ·1Al ₂ O ₃
P ₂	64SiO ₂ ·27CaO·4P ₂ O ₅ ·3TiO ₂ ·2Al ₂ O ₃

The crystallinity of the samples was investigated with Shimadzu XRD-6000 diffractometer using CuK α radiation ($\lambda = 1.54 \text{ \AA}$) and Ni filter. The diffractograms were recorded in the angular range $10^\circ \leq 2\theta \leq 80^\circ$ with a speed of $2^\circ / \text{min}$.

The study of morphology and elemental chemical composition was performed using scanning electron microscopy (SEM) with a Tescan Vega microscope equipped with an energy dispersive X-ray spectroscopy (EDX) detector enabling the assessment of the elemental concentrations in microscopic regions with a spatial resolution of several cubic micrometers.

RESULTS AND DISCUSSION

The X-ray diffraction analysis points out the non-crystalline state of samples after 600°C treatment. The large diffraction line recorded in a wide angle around $2\theta \sim 26^\circ$ (Fig. 1.a) consists of two components centered at 2θ values of 23.7° and 30.7° , assignable to glass network formers SiO₂ and P₂O₅, respectively. The assignment is supported by the most intense diffraction line of crystalline SiO₂ (JCPDSPDF No. 39-1425) and Ca₃(PO₄)₂ (JCPDSPDF No. 17-0498), respectively.

The SEM images of (66-x) SiO₂·27CaO·4P₂O₅·3TiO₂·xAl₂O₃ samples (Figs. 1. b-c) show porous particles with a varied morphology and dimensions between $500 \mu\text{m}$ and $1 \mu\text{m}$, as a result of the agglomeration of particles during the aging process.

On the surface of the larger granules can be observed smaller particles, which may be the result of the rearrangement in a new phase during the heat treatment (Fig.2.a-c-e). The precipitate has acicular or whiskers shapes or they appear as plates.

One notices that the acicular forms are prevalent in P₁ sample. This type of morphology is typical of hydroxyapatite development [17-20]. At the same time, the SEM images indicate the presence of interconnected fine particles that form irregular agglomerations.

EDX spectra collected from the sample's surfaces shown in Fig.2 a-c-e are shown in Fig.2.b-d-f and reflect their chemical elemental composition.

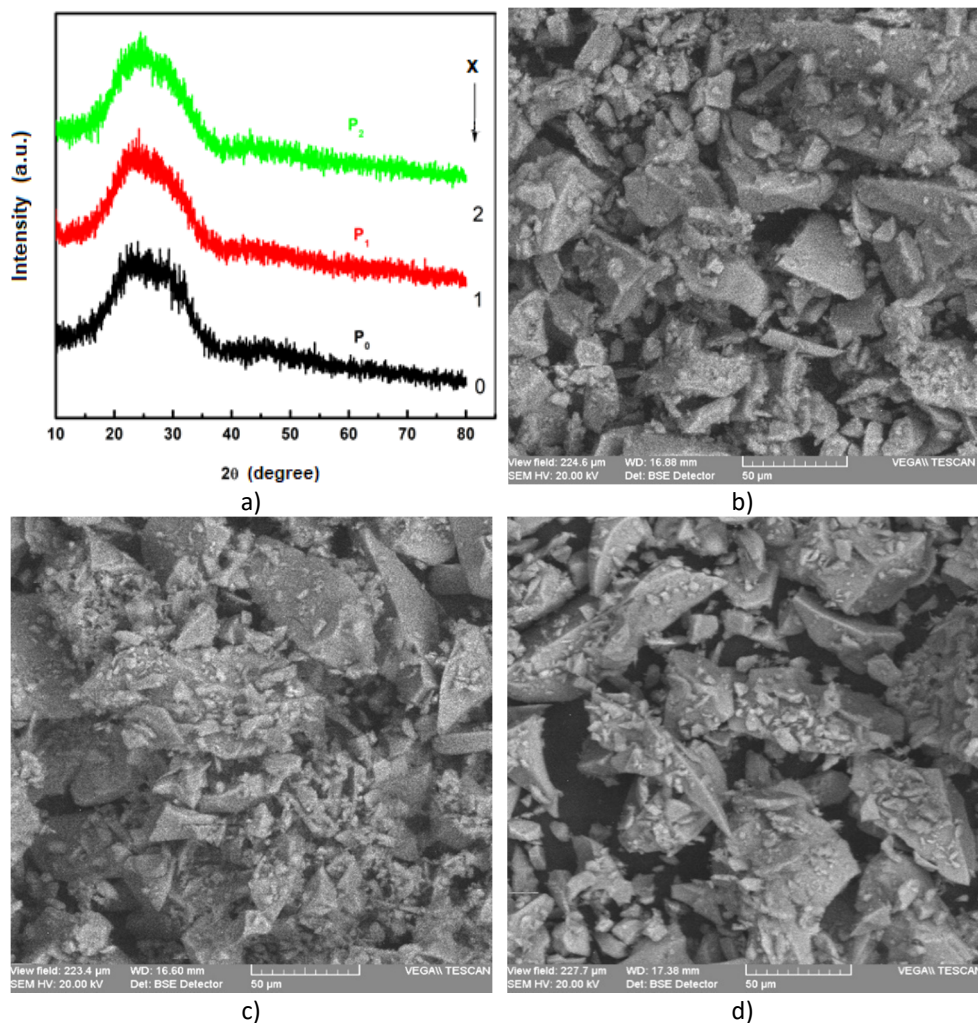


Fig. 1. Structure and morphology of glasses in the system $(66-x)\text{SiO}_2\text{-}27\text{CaO}\cdot 4\text{P}_2\text{O}_5\cdot 3\text{TiO}_2\cdot x\text{Al}_2\text{O}_3$:
 a) XRD patterns; b) SEM image of sample P₀ (x=0); c) SEM image of sample P₁ (x=1);
 d) SEM image of sample P₂ (x=2).

The elemental composition of Si, Ca, P, Ti, Al and O elements determined from EDX spectra (Fig. 2) is summarized in Table 2. Deviations from the nominal elemental concentration are observed for Si, Ca and Ti. According to nominal atomic compositions, for all samples prepared under the presented conditions, the Ca/P ratio is 3.375. A close value is obtained for P₀ sample, while for P₁ and P₂ samples, wherein Al₂O₃ was added, the Ca/P ratios are clearly lower, namely 2.03 and 2.63, respectively.

SYNTHESIS AND PRELIMINARY CHARACTERIZATION OF MODIFIED 45S5 BIOGLASSES

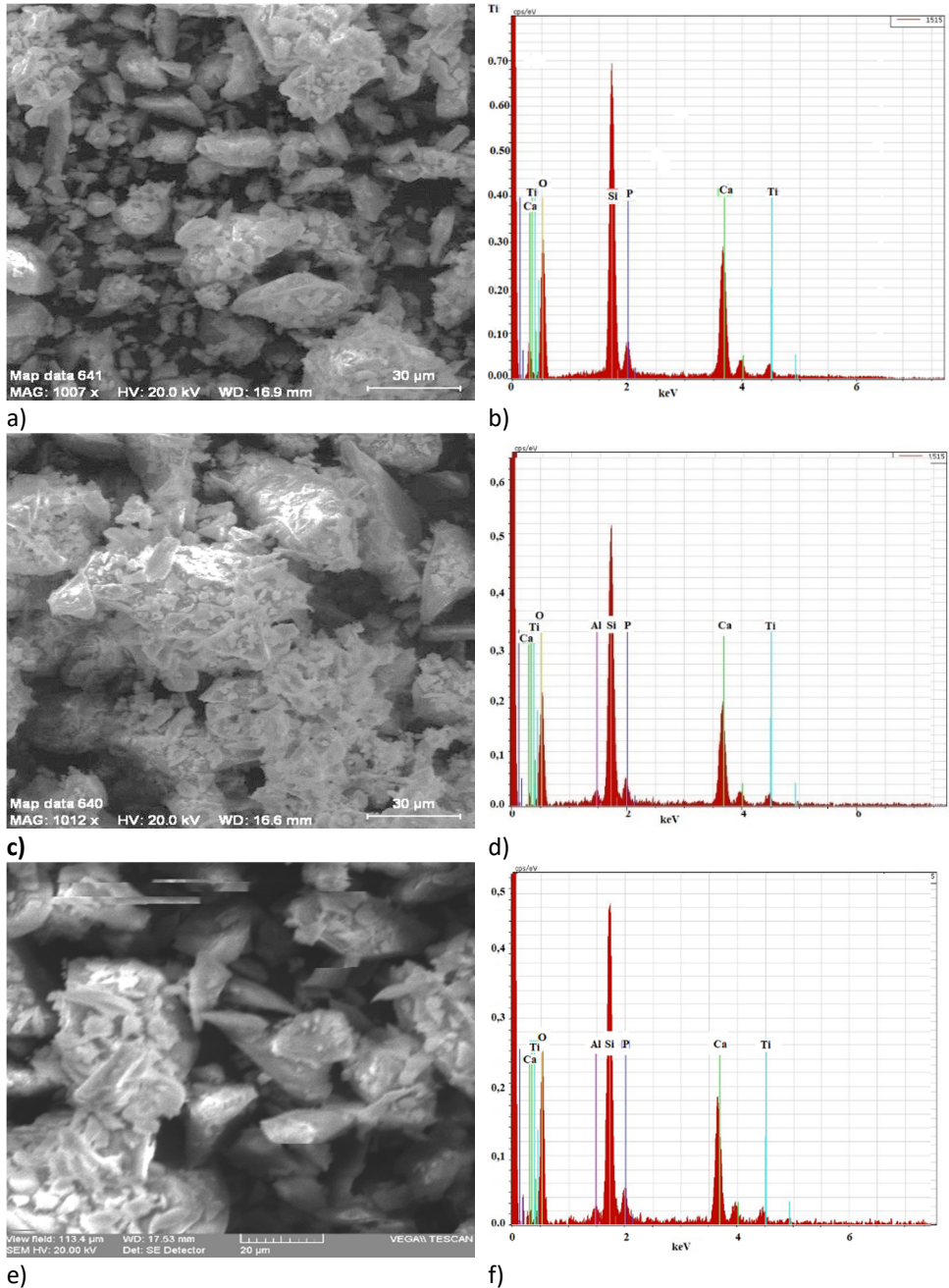


Fig.2. SEM images and corresponding EDX spectra for the studied samples: a) and b) P₀; c) and d) sample P₁; e) and f) sample P₂.

Table 2. Elemental composition (at %) and Ca/P ratio obtained by EDX analysis of sol-gel derived $(66-x)\text{SiO}_2 \cdot 27\text{CaO} \cdot 4\text{P}_2\text{O}_5 \cdot 3\text{TiO}_2 \cdot x\text{Al}_2\text{O}_3$ samples

Sample	Si	Ca	P	Ti	O	Al	Ca/P
P ₀	18,82	8,23	2,42	0,90	69,80	-	3,26
P ₁	23,12	5,83	2,86	0,55	66,40	1,24	2,03
P ₂	19,13	7,54	2,58	1,02	68,50	1,12	2,63

The decrease in the Ca/P could be related to the increase in the phase reach in P_2O_5 , favored, close to the hydroxyapatite reported for the bone tissue, by the aluminum oxide addition [21].

CONCLUSIONS

Samples of $(66-x)\text{SiO}_2 \cdot 27\text{CaO} \cdot 4\text{P}_2\text{O}_5 \cdot 3\text{TiO}_2 \cdot x\text{Al}_2\text{O}_3$ system ($x = 0, 1$ and 2 mol %) were prepared following the sol-gel route. Their structure was stabilized by 600°C treatment. The XRD analysis points out that all samples are non-crystalline, regardless of Al_2O_3 addition. The SEM images show porous particles shaped as plated and whiskers, with sizes between $1\text{-}500\ \mu\text{m}$. The acicular form is prevalent for the composition with $x = 1$ mol % Al_2O_3 . The elemental composition delivered by EDX analysis indicates for Ca/P ratio a close value to that of the nominal composition only for the sample without Al_2O_3 , and diminished values of Ca/P ratio in Al_2O_3 containing samples. The Ca/P ratios obtained after Al_2O_3 addition on account of SiO_2 are closer to that of natural hydroxyapatite reported for bone tissue, that is an attractive property for biomedical applications in orthopedics and dentistry.

REFERENCES

1. D. Ksouri, H. Khireddine, A. Aksas, T. Valente, F. Bir, N. Slimani, B. Cabal, R. Torrecillas, J. D. Santos, *NovaBiotechnol Chim* 17(2), 150(2018).
2. R. A. Jalil, K. A. Matori, M. H. M. Zaid, N. Zainuddin, M. Z. A. Khiri, N. A. A. Rahman, W. N. W. Jusoh, E. Kul, *J. Spectrosc.(Hindawi)* 9170412 (2020).
3. N. Kourkoumelis, I. Balatsoukas, M. Tzaphlidou, *J Biol Phys.*, 38(2), 279 (2012).
4. H. Zhang, B.W. Darvell, *Acta Biomaterialia*, 6 (8), 3216 (2010).
5. T. Kokubo, H. Takadama, *Biomater.*, 27, 2907 (2006).
6. D. Bellucci, A.Sola, R. Salvatori, A. Anesi, L. Chiarini, V. Cannillo, *Mater. Sci. Eng. C*, 43, 573 (2014).

7. D. Bellucci, A. Sola, M. Gazzarri, F. Chiellini, V. A. Cannillo, *Mater. Sci. Eng. C*, 33, 1091 (2013).
8. K. Magyari, R. Stefan, D.C. Vodnar, A. Vulpoi, L. Baia, *J. Non-Crystal. Solids* 402, 182 (2014).
9. K. Magyari, R. One, I.-S. Todor, M. Baia, V. Simon, S. Simon, L. Baia, *J. Raman Spectrosc.* 47, 1102 (2016).
10. M. Tamasan, H. Szilagyi, E. Vanea, V. Simon, *J. Optoelectron. Adv. M.* 15, 879 (2013).
11. J. R. Jones, *Acta Biomater.* 9, 4457 (2013).
12. E.A. Abou Neel, D.M. Pickup, S.P. Valappil, R.J. Newport, J.C. Knowles, *J. Mater. Chem.*, 19, 690 (2009).
13. L.L. Hench, J.M. Polak, *Science*, 295, 1014(2002).
14. L. L. Hench, *J. Am. Ceram. Soc.*, 74, 1487 (1991).
15. T. Kokubo, *Biomaterials*; 12, 155 (1991).
16. Carta D, Knowles JC, Smith ME, Newport RJ, *J Non-Cryst Solids*, 353, 1141 (2007).
17. P. Kiran, V. Ramakrishna, M. Trebbin, N.K. Udayashankar, H.D. Shashikala, *J. Adv. Res.*, 8, 279 (2017).
18. M. Taherian, R. Roaeeb, M. Fathi, M. Tamizifar, *J. Adv. Ceram.* 3(3), 207 (2014).
19. D. Ksouri, H. Khireddine, A. Aksas, T. Valente, F. Bir, N. Slimani, B. Cabal, R. Torrecillas, J. D. Santos, *Nova Biotechnol Chim* 17(2), 150 (2018).
20. L. Baia, M. Baia, W. Kiefer, J. Popp, S. Simon, *Chem. Phys.*, 327, 63 (2006).
21. O. Kaygili, Tatar, Y. S. Keser, *J. Sol-Gel Sci. Technol.* 65,105 (2013).

CROSS-CORRELATIONS IN THE BROWNIAN MOTION OF COLLOIDAL NANOPARTICLES

SZ. KELEMEN¹, L. VARGA¹, Z. NÉDA^{1,*}

ABSTRACT The two-body cross-correlation for the diffusive motion of colloidal nano-spheres is experimentally investigated. Polystyrene nano-spheres were used in a very low concentration suspension in order to minimize the three- or more body collective effects. Beside the generally used longitudinal and transverse component correlations we investigate also the Pearson correlation in the magnitude of the displacements. In agreement with previous studies we find that the longitudinal and transverse component correlations decay as a function of the inter-particle distance following a power-law trend with an exponent around -2. The Pearson correlation in the magnitude of the displacements decay also as a power-law with an exponent around -1.

Keywords: *colloidal particles, Brownian motion, cross-correlation.*

INTRODUCTION

In the last two decades, the dynamical behaviour of colloidal particles in the neighbourhood of an interface was frequently investigated [1]. The reason for the growing interest in such phenomena is that they might help in providing a better modelling framework for solving interesting problems such as 2D crystallization, crystal sublimation, interactions between similarly charged particles, Brownian dynamics at liquid interfaces and others [1-3].

Analysis of the Brownian dynamics in such restricted topologies allows also the investigation of more exotic diffusional processes with non-trivial scaling properties [4] and/or the micro-rheology of the fluid [2]. Differences from the motion of simple uncorrelated Brownian particles and consequently the presence of

¹ Babeş-Bolyai University, Faculty of Physics, 1 Kogălniceanu str., 400084 Cluj-Napoca, Romania.

* Corresponding author: zoltan.neda@ubbcluj.ro

some flow-mediated interactions are best revealed by means of well-constructed cross-correlated diffusion coefficients. Surprisingly, the involved correlations are long-ranged, decaying with the distance as a power-law with exponent -2. Their presence was explained in a simple manner by the two-dimensional dipolar form of the flow induced by the colloidal particles [3].

Colloids at the microscopic level were studied experimentally by means of digital video microscopy [5] and optical tweezers [6, 7]. Studies were conceived in different geometries: near a single wall [8, 9], between two walls (see for example [10] and references within), in a quasi-one-dimensional channel [11] or in a small container [12 and references within]. Colloids in confined spaces were also studied by Low Reynolds number simulations [13, 14] and a dynamic density functional theory [15]. Cui et al. [3] used digital video microscopy to demonstrate the drastic difference between the hydrodynamic interactions in a quasi-2D suspension both in a less confined and for a more confined system. Dufresne et al. [9] combined optical tweezer manipulation and digital video microscopy to investigate the diffusion of two colloidal spheres near a flat plate. The study demonstrates that even at large separations a confining surface can influence the colloidal dynamics.

The aim of the present study is to demonstrate once again the presence of the long-ranged correlation between the Brownian particles' displacements and estimate the exponent for the fat-tail. The novelty is, that besides the generally used cross-correlations in the perpendicular and parallel displacements, we measure also the cross-correlation for the scalar displacement of the particles and show that this has also a power-law decay.

EXPERIMENTAL SETUP AND METHOD

To study the phenomena, we used a method similar to the one described in the work of Greczyło et al. [16]. Controlled size polystyrene nano-spheres were dissolved in distilled water. The movement of the particles was recorded using an optical microscope with CCD camera connected to a laptop computer.

The system was prepared in the following manner: the polystyrene nano-spheres were suspended in distilled water. One drop of this suspension was placed on a silica glass slide and covered with a cover slip. By this way a quasi-two-dimensional geometry was achieved. Different sized nano-spheres were used, and for the same size several different experiments were considered. We used suspensions with low nanosphere concentration, in order to minimize three- or more body effects. We performed studies on nano-sphere suspensions with particle sizes: 607 nm, 1.5 μm and 2 μm .

In order to allow a HD resolution for the recordings, the frame-rate of the CCD camera was set to 15 frame/s. As an example, one recorded frame in case of the 2 μm nanoparticles is shown in Fig. 1. We performed quite long recordings, with total frame number of the order of 10^4 frames.

Tracking of the particles was done by a program written in Python. This tracking program uses a python package called *trackpy* [17] that extracts all the necessary information for an advanced statistical investigation of the particles dynamics. The program subtracts also any possible global drift flow. Such a global drift motion would lead to unrealistic correlations in the particles dynamics. Since the particle sizes were uniform in size up to 5%, we were primarily interested to track the x and y coordinates of each particle on each frame. As an example, a part of the data extracted by the program is shown in Table 1.

First, we have studied the generally used two particle cross correlations (covariance) for the longitudinal and transverse displacements.

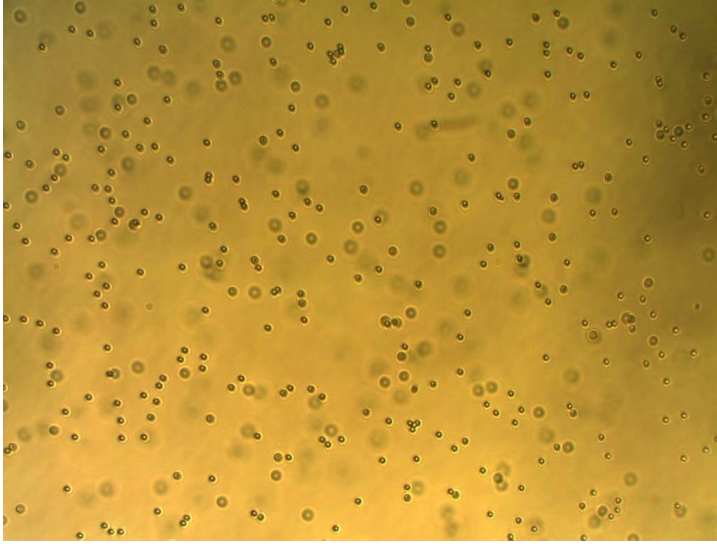


Fig. 1. Image obtained under the microscope in case of the 2 μm nanoparticles.

The z_q^{hk} covariance between particles h and k displacement is determined as

$$z_q^{hk} = \Delta r_q^k \Delta r_q^h, \quad (1)$$

where q can be \parallel or \perp , and the involved parallel and perpendicular displacements Δr_{\parallel}^k and Δr_{\perp}^k is sketched in Fig.2.

Table 1. Example for the data generated by the tracking program.

Data generated by the tracking program			
y	522.395	378.6569	174.9081
x	738.9558	76.9198	657.3284
mass	428.4899	404.0146	397.8096
size	3.1138	2.6762	3.0369
frame	0	0	0
particle	1	11	14

The time step considered for the displacements is the time-interval between the frames: $1/15 \text{ s} \approx 66.7 \text{ ms}$.

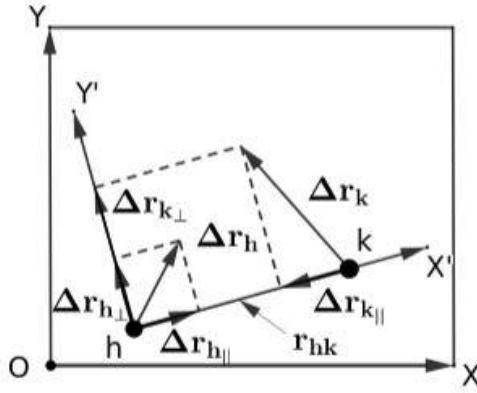


Fig. 2. Graphical representation of the parallel and perpendicular displacements relative to the direction connecting the two particles.

The particles in our setup have a spherical geometry, and their diameter has a relative difference less than 5%. Due to the relatively small density, by neglecting the three or more body effects, we expect that the magnitude of this covariance is influenced only by the inter-particle distance $s = r_{kh}$. In order to determine the decay of this covariance as a function of the inter-particle distance we average on all pairs of particles on all consecutive frames where it is found an inter-particle distance: $r_{kh} \in [s - \Delta, s + \Delta]$:

$$z_q(s) = \langle \Delta r_q^k \Delta r_q^h \rangle_{\{k,h|r_{kh} \in [s-\Delta, s+\Delta]\}} \quad (2)$$

Here the value of Δ is suitable chosen so that we remain with enough bins and also there are many (more than 1000) occurrences in each bin. Earlier studies [1] suggested that in a quasi 2D topology the covariance $z_q(s)$ decay as a function of s in form of a power-law with exponent close to -2.

In the present study, we consider yet another correlation ($z_{|\Delta r|}$), dealing with the magnitude of the particles displacements. This cross-correlation is determined by the simple Pearson correlation coefficient [18] defined as:

$$z_{|\Delta r|}(s) = \frac{\langle |\Delta r_k| |\Delta r_h| \rangle_n - \langle |\Delta r_k| \rangle_n \langle |\Delta r_h| \rangle_n}{\sigma_n(|\Delta r_k|) \sigma_n(|\Delta r_h|)} \quad (3)$$

where n indicates the same averaging that was considered for $z_q(s)$, i.e. $n \equiv r_{kh} \in [s - \Delta, s + \Delta]$

EXPERIMENTAL RESULTS

The amount of processed data (number of frames and detected number of particles) are summarized in Table 2. For a given nanosphere size we have combined the data for all the performed experiments in order to obtain a final scaling with improved statistics. The obtained results for the scaling exponents and for the R^2 correlation coefficient is given in Table 3. The results are in good agreement with the ones recently published in [1].

Table 2. The amount of the processed data: the number of frames and detected particles.

Experiments			
Experiment	Part. diam.	No. of frames	Tot. no. of part.
1	607 nm	8000	18314
2	607 nm	12506	40635
3	607 nm	7498	23550
4	607 nm	8000	26464
5	607 nm	8000	22111
6	1.5 μm	7498	7392
7	1.5 μm	6288	4946
8	2.0 μm	2328	19223
9	2.0 μm	2240	19981
10	2.0 μm	8500	19088
11	2.0 μm	3524	2082
12	2.0 μm	14429	8877
13	2.0 μm	14843	8027

In order to illustrate the power-law decay of $z_q(s)$ we present it on log-log scales in case of the 1.5 μm -sized particles. On Fig.3 we plot the results for the longitudinal components and on Fig.4 for the transverse components. In studying

the perpendicular and transverse covariance (2) we have chosen the size of the bins as $2\Delta = 2 \mu m$ and $2\Delta = 3 \mu m$, respectively. For studying the correlation between the particles displacements (3) the bin size was chosen as $2\Delta = 2 \mu m$ and the obtained trend for $z_{|\Delta r|}$ is plotted in Fig.5.

In all cases the correlation was detectable until a reasonable large s inter-particle distance of around $50 \mu m$. We obtained similar results for the covariance in the case of 607 nm - and $2 \mu m$ -sized particles (see Table 3).

The Pearson correlation coefficient (3) as a function of the inter-particle separation distance exhibits also a power-law trend with a scaling exponent very close to -1 . The statistics of the data and the obtained scaling exponents are summarized in Table 4.

Table 3. The statistics of the processed data and results for the longitudinal and transverse covariance (2).

Longitudinal covariance				
Part. diam.	No. of frames	Tot. no. of part.	Scaling exponent	R^2
607 nm	28004	82499	-1.940	0.876
1.5 μm	13786	12338	-2.061	0.970
2.0 μm	43624	57297	-1.940	0.856
Transverse covariance				
Part. diam.	No. of frames	Tot. no. of part.	Scaling exponent	R^2
607 nm	28004	82499	-1.583	0.786
1.5 μm	13786	12338	-2.004	0.962
2.0 μm	43624	57297	-2.137	0.689

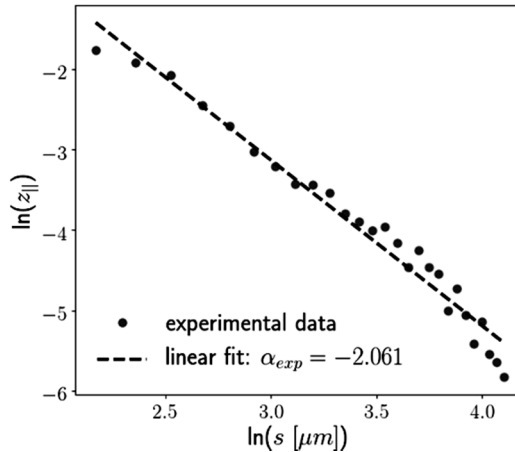


Fig. 3. The covariance for the longitudinal displacement as a function of the interparticle distance (s) in case of the $1.5 \mu m$ -sized particles.

Table 4. The statistics of the processed data and results for the Pearson correlation between the particles displacement.

Pearson correlation				
Part. diam.	No. of frames	Tot. no. of part.	Scaling exponent	R^2
607 nm	16000	48575	-0.756	0.796
1.5 μm	13786	12338	-0.998	0.926
2.0 μm	13068	58292	-0.639	0.712

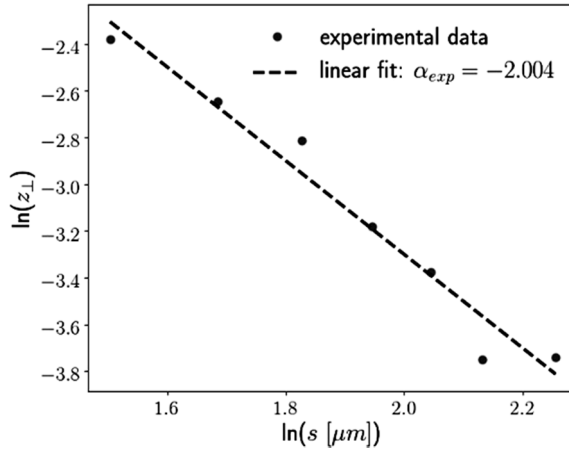


Fig. 4. The covariance for the transverse displacement components as a function of the interparticle distance (s) in case of the 1.5 μm -sized particles.

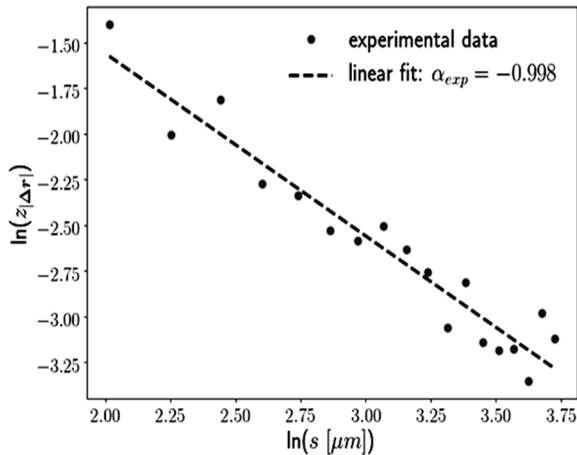


Fig. 5. The Pearson correlation for the magnitude of the displacements as a function of interparticle distance (s) in case of the 1.5 μm -sized particles.

CONCLUSIONS AND DISCUSSION

We confirmed that the Brownian like motion of colloidal nanoparticles restricted to a quasi 2D geometry exhibits two-particle cross-correlation decaying as a power-law. For the covariance of the longitudinal and transverse displacements we got a decay exponent similar to the one suggested by earlier studies, close to the value of -2 (Table 3). We have shown that the magnitude of the particles displacements is also correlated, and the Pearson type correlation decays with the interparticle separation distance much slower, as a power-law with an exponent very close to -1. In case of the longitudinal and transverse correlations the values of the exponents are in good agreement with the prediction of a simple hydrodynamic argument [3]. The statistics for the goodness of the power-law fit indicated the largest R^2 value for the experiments performed with the 1.5 μm sized particles. The lowest R^2 values were around 0.7, and were obtained for the experiments performed with the 2 μm size nanospheres.

ACKNOWLEDGEMENT

The work of Sz. Kelemen was supported by the Research Performance Scholarships of the Babeş-Bolyai University. We acknowledge the help of CP1. Dr. M. Focşan from UBB, who provided us the microspheres for the experiments. Z. Neda acknowledges financial support from the UEFSCDI grant PN-III-P4-PCE-2016-0363.

REFERENCES

1. W. Zhang, N. Li, K. Bohinc, P. Tong, W. Chen, *Phys. Rev. Lett.* **111**, 168304 (2013).
2. N. Li, W. Zhang, Z. Jiang, W. Chen, *Langmuir* **34**, 10537 (2018).
3. B. Cui, H. Diamant, B. Lin, S. Rice, *Phys. Rev. Lett.* **92**, 258301 (2004).
4. B. Tóth, B. Valkó, *Journal of Statistical Physics*, **147**, 113 (2012).
5. E. Weeks¹, J. Crocker, D. Weitz, *J Phys.-Condens. Mat.* **19**, 205131 (2007).
6. L. A. Hough, H. D. Ou-Yang, *Phys. Rev. E* **65**, 021906 (2002).
7. J. C. Meiners, S. R. Quake, *Phys. Rev. Lett.* **82**, 2211 (1999).
8. G. S. Perkins, R. B. Jones, *Physica A* **189**, 447 (1992).
9. E. Dufresne, T. Squires, M. Brenner, D. Grier, *Phys. Rev. Lett.* **85**, 3317 (2000).
10. E. R. Dufresne, D. Altman, D. G. Grier, *Europhys. Lett.* **53**, 264 (2001).
11. B. Cui, H. Diamant, B. Lin, *Phys. Rev. Lett.* **89**, 188302 (2002).
12. M. P. Brenner, *Phys. Fluids* **11**, 754 (1999).
13. R. Pesche, G. Nagele, *Europhys. Lett.* **51**, 584 (2000).
14. J. P Hernandez-Ortiz, P. T. Underhill, M. D. Graham, *J. Phys: Cond. Mat.* **21**, 204107 (2009).
15. L. Almenar and M. Rauscher, *J. Phys: Cond. Mat.* **23**, 184115 (2011).
16. T. Greczyło, D. Ewa. *Proc. MPTL* **9** (2004).
17. Trackpy, URL: <http://soft-matter.github.io/trackpy/stable/tutorial/walkthrough.html> (accessed 14 Jul. 2019)
18. K. Pearson, *P. R. Soc. London*, **58**, 240 (1895).

ATTOSECOND INTERFEROMETRY USING A HHG- $2\omega_0$ SCHEME*

V. LORIOT^{1,**}, A. MARCINIAK¹, S. NANDI¹, G. KARRAS¹, M. HERVÉ¹,
E. CONSTANT¹, E. PLÉSIAT², A. PALACIOS², F. MARTIN², F. LÉPINE¹

ABSTRACT. We present an interferometric HHG- $2\omega_0$ scheme and compare it to the usual XUV-IR RABBIT method that is widely used in attosecond science. Both methods are able to reconstruct the properties of an attosecond pulse train and can be used to measure attosecond ionization time delays in atoms and molecules. While they have several similarities, they also have conceptual differences. Here, we present some particularities of the HHG- $2\omega_0$ method and its advantages and drawbacks, which would help to define situations where it can provide information inaccessible by other technics.

Keywords: Attosecond, Photoionization, RABBIT

INTRODUCTION

With the advent of attosecond science ($1 \text{ as} = 10^{-18} \text{ s}$), it is now possible to have access to the natural timescale of electronic motion [1,2]. The extreme-ultraviolet (XUV) one-photon ionization of an atom or a molecule produces an electron in the continuum with a kinetic energy that depends on the interaction properties with the ionic core [3]. While the electron escapes, it experiences the interaction with its parent ion, and it can therefore be used as a probe of the ionic potential. Depending on these forces, the emitted electron can be attracted (*resp.* repelled) by the potential, which can be interpreted as an advance (*resp.* delay) on the ionization time. Such electron dynamics contain the details of the fundamental photoelectric process, thus unravelling the structure of the continuum of an atom or a molecule [4].

* Presented at the First Annual Workshop for the COST Action Attosecond Chemistry (ATTOCHEM) CA18222, organized on-line, September 9-11, 2020.

¹ Univ Lyon, Univ Claude Bernard Lyon 1, CNRS, Institut Lumière Matière, F-69622, VILLEURBANNE, France.

² Departamento de Química, Modulo 13, Universidad Autónoma de Madrid, 28049 Madrid, Spain, EU.

** Corresponding author: vincent.loriot@univ-lyon1.fr

Nowadays, it is experimentally possible to observe electron dynamics in time-resolved experiments, thanks to the development of High-order Harmonic Generation (HHG). HHG provides a table-top solution to produce attosecond pulses with a high degree of reproducibility and an intrinsically low temporal jitter between the XUV and the fundamental pulse. One way to probe attosecond dynamics is the RABBIT (Reconstruction of Attosecond Beating by Interference of Two-photon Transitions) method [5]. It employs an attosecond pulse train (APT) generated by HHG in gas, spatio-temporally overlapped with a perturbative dressing field. Both beams are produced with the same femtosecond laser source at the central frequency (ω_0). Measuring the photoelectrons resulting from the interaction between an atomic or molecular target with XUV pulses with attosecond accuracy allows measuring the photoionization time delay with both temporal and spectral resolution [6]. This powerful method has demonstrated its relevance in many physical systems [6-9]. The method is well suited for small atomic targets that can usually be considered as a single active electron system. However, for more complex targets, with more than one active electron and with extra degrees of freedom, this method can still work [8] but suffers from a rapid congestion of the experimental signal [10].

Recently, we proposed a variant of the RABBIT method that allows the experimental separation of the attosecond dynamics of a two active electron system [11]. The principle is to use a $2\omega_0$ dressing photon energy (instead of ω_0 for the RABBIT method) to avoid introducing new features (sidebands) in the XUV induced photoelectron kinetic energy spectrum (KES). Following this scheme, the photoelectron KES does not significantly vary with the XUV- $2\omega_0$ delay. Nevertheless, the attosecond information remains encoded in the angle of ejection of the electron in the laboratory frame. Hence, it becomes possible to recover the attosecond information by measuring the angularly resolved photoelectron KES as a function of the relative delay between the two pulses. This can be performed using a velocity map imaging (VMI) spectrometer [12] that is well suited for this purpose. The measurement of the time-resolved anisotropy parameter allows for the reconstruction of the electron dynamics.

This method can be used as an alternative approach to the RABBIT technique to both reconstruct the attosecond pulse train [13] and the photoionization time delays in molecules [11]. This scheme is not limited to the experimental arrangement presented here, it can also take place under different experimental configurations. For instance, an equivalent configuration can be obtained by generating both even and odd harmonics (HHG_{even+odd}) dressed by a perturbative pulse centered around ω_0 . HHG_{even+odd} can be performed in a gas target using a pulse composed by a

combination of ω_0 and $2\omega_0$ carrier fields locked in phase [14,15]. Also HHG_{even+odd} can be generated in a non-centrosymmetric media such as HHG from plasma mirror [16]. Time resolved photoelectron measurements obtained by the interaction of an HHG_{even+odd} dressed by an ω_0 photon is equivalent to the HHG- $2\omega_0$ presented here (*i.e.* HHG_{odd-only}- $2\omega_0$). In both cases, the dressing field couples the consecutive harmonics to each other.

In the present work, we first present the HHG- $2\omega_0$ method in details: its experimental implementation, the produced signal, its particularities, and specific analysis. Second, we show an example of extraction of the ionization phase differences between two electronic states from an experimental signal. Finally, the differences with the RABBIT method are discussed.

METHOD

HHG in gas targets generated by a linearly-polarized femtosecond laser pulse centered around the central frequency (ω_0) results in a spectral comb composed by odd harmonics of the fundamental laser frequency due to the centrosymmetric configuration [17]. Such harmonics are separated by twice the fundamental frequency ($2\omega_0$). HHG is a non-perturbative process, where the n^{th} order high harmonic yield does not follow the non-linear perturbation rule ($\text{yield} \propto I^n$), but the high harmonics can have similar intensities leading to an intensity plateau up to the cut-off energy given by $E_{\text{max}} = Ip + 3.2Up$ [18] (with Ip the ionization potential of the generating atom and Up the ponderomotive energy). Using a fundamental central frequency (ω_0) in the near infra-red ($\hbar\omega_0$ up to ~ 1.5 eV), HHG leads to a frequency comb in the XUV range ($\hbar\omega_{\text{XUV}} > 10$ eV). Since such harmonics are phase locked, the comb can correspond, in the temporal domain, to an attosecond pulse train (APT) [5,19].

The interaction of this APT with a single active electron system can lead to the ionization of the target because the XUV-photon energy is usually above the ionization potential of atoms and molecules. In the photoelectron KES, it results in peaks around the difference between the photon-energy and the ionization potential of the target ($\hbar\omega_{\text{XUV}} - Ip_{\text{target}}$). The measurement of the resulting angularly resolved photoelectron KES by itself (*cf.* Fig. 1(a,d)) does not allow to reconstruct the phase of the emitted photoelectron wave packet because it corresponds to a squared modulus of the amplitude probability. The traditional way to access phase information relies on the use of interferometric technics. To this aim, it is possible to use a weak dressing field that couples the ionization channels. Hence, quantum interferences can take place and they carry the information on the relative phases of the electron wave packets. The attosecond information can be retrieved by scanning the linear spectral phase of the dressing pulse, which corresponds, in the

time domain, to the delay between the APT and the dressing pulse. The RABBIT method proposes to use a single ω_0 photon to couple ionization channels between each other (Fig. 1(b,e)). This has the advantage to produce a signal on an *a priori* “background-free” photoelectron region and all the relevant information is gathered in the phase of the oscillation of the electron signal intensity. In contrast, the HHG- $2\omega_0$ method uses a single $2\omega_0$ photon field to couple the ionization channels (Fig. 1(c,f)). In this case, the oscillating signal is no longer measured on background-free conditions, and no significant changes can be observed in the angularly integrated photoelectron KES. However, the attosecond information remains present, and the oscillation appears as an asymmetric redistribution of the electron signal on each side of the laser polarization axis (vertical in Fig. 1). The electrons are preferentially redistributed either on the upper or lower side in the laboratory frame, involving odd β terms (β_{odd}) of the Legendre polynomial expansion to describe the photoelectron angular distribution [20]. This asymmetry oscillates with respect to the delay between the APT and the dressing pulse frequency ($2\omega_0$).

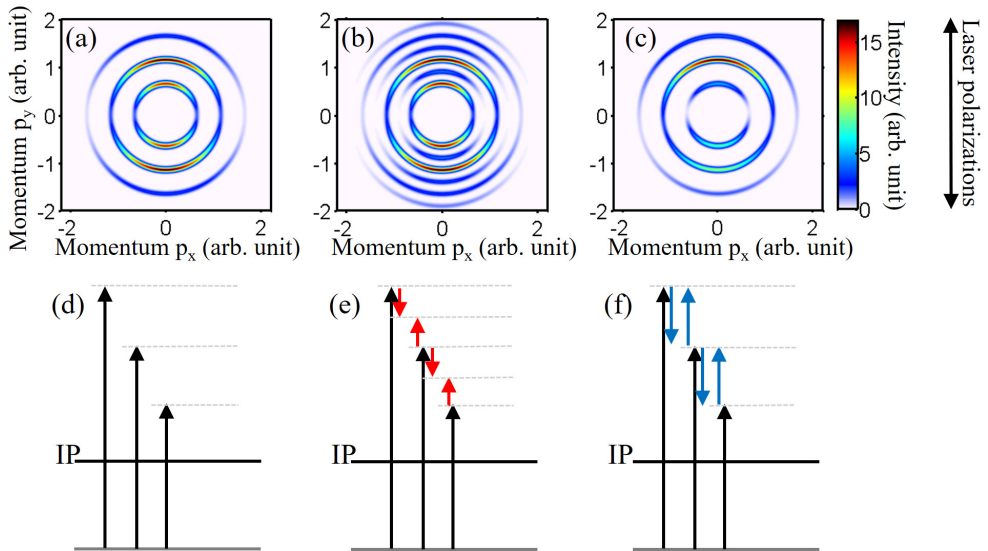


Fig. 1 (a-c) Numerical simulation of the angularly resolved photoelectron distribution with a vertical polarization (along the p_y -axis) of the pulses where the APT pulse is (a) alone, (b) dressed by an ω_0 photon (RABBIT-scheme) and (c) dressed by a $2\omega_0$ photon (HHG- $2\omega_0$ configuration). (d-f) Energetic diagram corresponding respectively to (a-c). The harmonics (vertical black arrows) are ionizing an electronic state (gray solid line) to the continuum. The dressings photons (red arrows for RABBIT and blue arrows for HHG- $2\omega_0$) lead to the one-photon energy redistribution of the photoelectrons. Interferences occur at the energies indicated by horizontal dotted lines.

In the present work, we consider the HHG- $2\omega_0$ process under the lowest order of perturbation theory (i.e. weak dressing field). In this case, the resulting electron wave function depends on several ionization paths. The derivation of the dipole transition has been presented in Laurent *et al.* [14,15,21]. Different paths can lead to a given final photoelectron energy (see Fig.1(f)) as summarized in Table 1:

Table 1. Summary of the photo-absorption paths at the lowest order of perturbation theory, and the paths combinations that lead to a specific oscillating term in the interference.

Paths	$\hbar\omega_{XUV}$	(i)
	$\hbar\omega_{XUV} + \hbar\omega_{dress}$	(ii)
	$\hbar\omega_{XUV} - \hbar\omega_{dress}$	(iii)
Interferences	(i) +(ii) : β_{odd} ; Yield=constant ; Oscillation $2\omega_0$	(1)
	(i) +(iii) : β_{odd} ; Yield=constant ; Oscillation $2\omega_0$	(2)
	(ii)+(iii) : β_{even} ; Yield=vary ; Oscillation $4\omega_0$	(3)

(i)The direct absorption of an XUV photon ($\hbar\omega_{XUV}$), (ii) the absorption of an XUV photon and a dressing photon ($\hbar\omega_{dress} = 2\hbar\omega_0$), and (iii) the absorption of an XUV photon with a stimulated emission of a dressing photon. The interference (1) between the paths (i) and (ii) involves paths with a different number of photons. This results in an asymmetrical redistribution of the electron angular distribution with respect to the polarization axis (only β_{odd}) maintaining constant the yield (2π angular integration of the photoelectron distribution). The corresponding oscillation is expected at the dressing field frequency ($2\omega_0$). A similar scheme appears in the interference (2), between the paths (i) and (iii) producing electrons at the same final kinetic energy.

The interference (3) can take place between the paths (ii) and (iii). This interference corresponds to the RABBIT-like scheme, as shown in Fig.1 (e) where the central harmonic does not play any role. This interference is significantly different from the interferences (1) and (2) because, in this case, both paths involve the same number of photons leading to an interference that significantly changes the photoelectron KES. Since the transition parity is preserved, a symmetric redistribution of the electrons on each side of the polarization axis (β_{even}) is expected. This pattern may oscillate at twice the dressing field photon energy, hence at $4\omega_0$. The interference (3) can easily be distinguished from the interferences (1) and (2) by measuring the oscillation frequency and the electron ejection anisotropy. Moreover, the interference (3) is expected to appear at higher dressing field intensity because more than one-dressing photon is involved in the process.

The interferences (1) and (2) can be treated separately, their resulting intensities are summed up [14]. The asymmetric oscillation $\Delta S_n(t)$ of the angular distribution that appears on the top of the XUV-only harmonic peaks (of the order n) can be written as:

$$\Delta S_n(t) = \frac{A_n A_{n-2} \cos(2\omega_0 t + \varphi_{n-2} - \varphi_n) - A_{n+2} A_n \cos(2\omega_0 t + \varphi_n - \varphi_{n+2})}{}, \quad (4)$$

with t being the delay between the APT and the dressing pulse ($t > 0$ corresponds to a dressing pulse that arrives later). A_n and φ_n are respectively the amplitude and phase of the one-photon ionization following the absorption of the n^{th} order harmonic. Similarly, $A_{n\pm 2}$ and $\varphi_{n\pm 2}$ denote the corresponding amplitude and phase of the two-photon ionization following the absorption of a photon at the harmonic order $n\pm 2$ accompanied with the one-photon emission or absorption of the dressing field. The amplitudes A depend on the photo-absorption cross-section and the HHG and dressing field intensity. The phases φ contain the dipole transition phase, the harmonics phase and the Coulomb interaction phase. The two contributions are oscillating at $2\omega_0$ frequency, so their sum also oscillates at the $2\omega_0$ frequency. The experimental signal $S_n(t)$ at the harmonic location n can hence be re-written as a simple oscillation as follows:

$$S_n(t) = B_n \cos(2\omega_0 t + \phi_n), \quad (5)$$

where B_n and ϕ_n are respectively the global oscillation amplitude and phase on the top of the harmonic n . Only B_n and ϕ_n terms are experimentally measurable by recording the time-resolved photoelectron KES on one side of the laser polarization axis. The measurable parameters (B_n and ϕ_n) are both depending on 6 parameters ($A_n, A_{n-2}, A_{n+2}, \varphi_n, \varphi_{n+2}, \varphi_{n-2}$).

As a comparison, in the usual RABBIT method, an oscillation of the yield is observed in the sidebands with respect to the delay between the pulses. The sideband oscillation phase can be established from the phases φ_{n+1} and φ_{n-1} , and the sideband oscillation amplitude from the amplitudes A_{n+1} and A_{n-1} . At the lowest order of perturbation theory, the dressing field does not ionize, but redistributes the photoelectron intensity over different electron kinetic energies. Hence the RABBIT photoelectron yield on the harmonics peaks (bands) are also oscillating maintaining constant the total ionization yield. The oscillation of such bands depends on the interferences with the surrounding sidebands. Therefore, this band oscillation is comparable with the one of HHG- $2\omega_0$ method, because its expression is similar to the

one presented in Eq. 4 with both terms negative (not only the second one). In the RABBIT method, despite that all the relevant information can be extracted from the sideband oscillation amplitude and phase, the analysis of the bands can also be used to refine the reconstruction due to the redundancy of the information [22]. Both bands and sidebands indeed encode the same (A, ϕ) parameters in a different way.

The correspondence between (A, ϕ) and (B, ϕ) is not straightforward. The measured (B, ϕ) can dramatically change by slightly changing (A, ϕ) . The (A, ϕ) terms can both be set experimentally using XUV optics such as metallic filters [23] that can modify the harmonic distribution and/or its spectral phase. In the following, we show the typical changes in (B, ϕ) due to amplitude (Fig. 2(b,e)) and phase (Fig. 2(c,f)) shaping, from a reference condition (Fig. 2(a,d)).

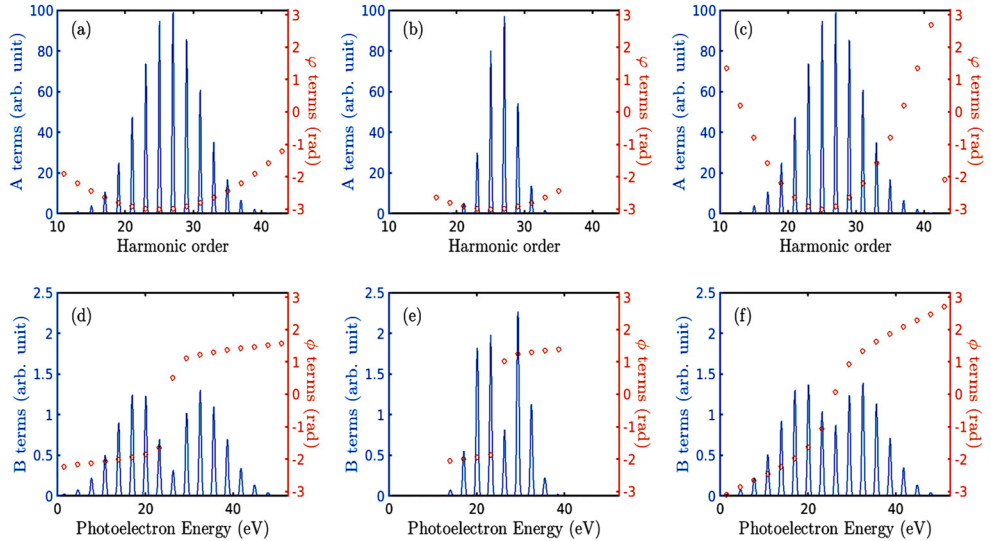


Fig. 2. Numerical simulation of Eq. 4 corresponding to the HHG- $2\omega_0$ method. (a-c) are the (A, ϕ) terms in solid blue line and orange circles respectively. (b) corresponds to an amplitude narrowing of (a), (c) four times stronger parabolic spectral phase compared to (a). (d-f) The corresponding amplitude B (blue) and phase ϕ (orange) of the $2\omega_0$ oscillation using the respective spectra shown in (a-c). In the simulation, the ionization potential has been chosen to be 15.6 eV (close to the I_p of N_2 and Ar), and $\hbar\omega_0=1.55$ eV.

The reference (A, ϕ) condition shown in Fig. 2(a) represents a comb of harmonics with a Gaussian envelope and a small quadratic spectral phase (chirp) of 2000 as^2 . Its corresponding oscillation, (B, ϕ) terms, are shown in Figure 2(d). The chirp appears as a linear distribution of the ϕ phase terms due to the consecutive phases

differences in Eq. (4). On the top of this tendency, a phase-jump (about π) appears close to the maximum of the Gaussian envelope. It corresponds to a sign change in the equation (4) where the term $(A_{n-2}-A_{n+2})$ becomes positive or negative (*i.e.* $-1=e^{i\pi}$). This implies a change in the most intense term in Eq. 4. In a first approximation, the B term distribution follows the product between the Gaussian envelope and its derivative, showing the highest oscillation where the slope of the envelope is pronounced.

The narrowing of the A distribution by a factor of 4 (maintaining φ shape constant) leads to significant changes in both (B, ϕ) terms (see Figure 2 (b) and (e)). The linear slope in φ_n is still apparent, and the phase-jump is more pronounced due to a sharper difference between the $(A_{n-2}-A_{n+2})$ coefficients. The B amplitudes distribution is narrowed and more pronounced compared to the reference due to a significant change in the (A_{n-2}/A_{n+2}) ratio. A moderate narrowing of the A terms can lead to a very different set of (B, ϕ) terms.

An increase by a factor 4 of the quadratic chirp (maintaining the A terms distribution) also leads to significant changes in both (B, ϕ) terms (see Figure 2 (c) and (f)). The resulting phases φ are linearly increasing with a stronger slope with a smooth phase-jump. On the other hand, the oscillation amplitudes B are enhanced compared to the reference because the terms in equation 4 do not efficiently cancel each other.

In general, the use of an XUV filter affects both the amplitude and the phase of the harmonics that directly modify the (A, φ) set. Such changes can dramatically affect the (B, ϕ) distributions due to the coupling between the parameters. Let us notice that the flat phase case over an A terms plateau produces the lowest oscillation amplitude B increasing required performances of the experiment. This flat phase case is usually sought because it corresponds to the shortest attosecond bursts (when atomic/molecular effects are weak).

In order to characterize a light-matter interaction, it is usually necessary to reconstruct the amplitude and the phase terms (A, φ) from an experimental measurement (B, ϕ) . This task is not straightforward because of the high dimensionality of the problem and the correlation between the parameters. An experimental example is presented in the following.

EXPERIMENT

In a recent work, we used the HHG- $2\omega_0$ strategy to extract the relative ionization time delay between two electronic states of the N_2 molecule [11]. The two uppermost levels, the X -state ($^2\Sigma_g^+$, $Ip_X=15.6$ eV) and the A -state ($^2\Pi_u$, $Ip_A=16.98$ eV) in N_2^+ ions are separated from each other by 1.4-1.7 eV in the photoelectron KES,

depending on the vibration level of the A-state. Following a standard RABBIT protocol using a standard Ti:Sa femtosecond-Laser as a seed ($\hbar\omega_0 \approx 1.5$ eV), the bands of an electronic state can overlap with the sidebands of the other electronic state [24]. In that case, an HHG- $2\omega_0$ protocol is well suited to separate the dynamics of the electronic states of this molecule.

In the X-state of N_2^+ , a shape resonance appears at photon energy around 30 eV [25]. The shape resonance has two consequences, first the absorption cross-section experiences a maximum and second the phase of the escaping electron is significantly affected. A rapid change in the phase (φ), as a function of the photon energy (E), can be interpreted as a delay in the photoionization time, following the Wigner theory [26] $\tau_w = \hbar \partial \varphi / \partial E$. Since the X and A states are measured in similar experimental conditions, all the sources that affect the observations (phase of the harmonics, continuum-continuum phase, ...) can be considered as identical. The energy difference between the two states is small, and the A state has no resonance in this spectral region ($\tau_w(A) \approx 0$). Therefore, it is possible to use the A-state as a reference to measure the dynamics induced by the shape resonance in the X-state.

The experimental measurement is shown in Fig. 3. The measurement shown in Fig.3(a) represents the photoelectron distribution angularly integrated over the upper part of the VMI detector (over the range $[-\pi/2 : \pi/2]$ with respect to the laser polarization axis) as a function of the time delay between the XUV and the dressing pulse. Since the attosecond oscillations represent only a few percent of the overall signal, the photoelectrons generated by the XUV-pulse measured alone have been subtracted to highlight the oscillating part of the signal in Fig. 3(a).

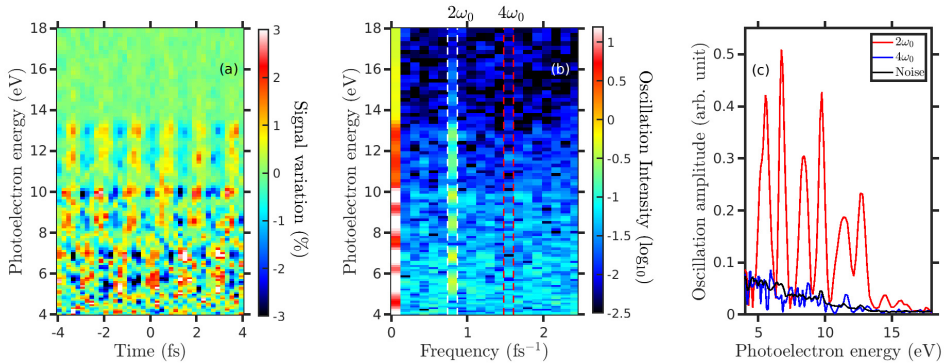


Fig. 3. (a) HHG- $2\omega_0$ measurement in N_2 (adapted from [11]) and (b) its corresponding Fourier transformation resolved in kinetic energy. (c) Amplitude of oscillation at $2\omega_0$ (red) and $4\omega_0$ (blue) compared to the mean oscillation amplitudes (black) of the Fourier transformation at other frequencies.

The Fig. 3 (b,c) shows the amplitudes of the oscillations as a function of the photoelectron energy. The oscillation amplitudes are extracted by performing a Fourier transformation of the temporal signal for the measured kinetic energies considered individually. Note that the amplitude is in log-scale which illustrates the difference in two orders of magnitude between the XUV-only photoelectron distribution (frequency=0 fs⁻¹) and the HHG-2 ω_0 oscillation (frequency=0.75 fs⁻¹, *i.e.* period of 1.33 fs). Fig. 3(c) shows the oscillation amplitude in a linear scale and compares them with the estimated noise level that is taken as the mean oscillation amplitude of the other frequencies (all frequencies except 0, 0.75 and 1.5 fs⁻¹). This figure shows a SNR of about 10 between the amplitude of oscillations at 2 ω_0 compared to the estimated noise level. It can be noticed that no oscillation is observed at the 4 ω_0 -frequency (frequency=1.5 fs⁻¹, *i.e.* period of 666 as). This indicates that the dressing field is weak enough and does not produce significant RABBIT-like oscillations in the observable (interference path (3)).

In order to extract the ionization phases of the X and the A states of N_2 , it is necessary to reconstruct the (A, φ) terms from both (B, ϕ) terms extracted from the measurement shown in Fig. 3. An analytical reconstruction solution of the φ terms has been proposed by Laurent *et al.* [15] (iPROOF) from the experimental (B, ϕ) assuming that the A terms are measured separately. In principle, the A distribution can be associated to the photoelectron KES measured when the XUV pulse is alone. In our case, we do not strictly follow this principle because the focal size of the harmonics depends on their wavelength leading to a different effective overlap with the dressing field. In our case, the A terms are considered as free parameters, but the reconstructed effective HHG spectrum may gradually follow the directly measured HHG distribution. The reconstruction is given by an optimization algorithm that directly uses the equation 4. The determination of the initial guess is critical due to the presence of several local optimums in the optimization landscape.

Figure 4 shows the result of the extraction of the relative ionization phase between the X and A -states in N_2 . The reconstruction of (A, φ) is performed for the two states considered separately. The experimental B term (Fig. 4(a)) is defined by integrating the oscillation over the peak width. The corresponding experimental phase is the center of mass of the phase over the width of the peak weighted by the oscillation amplitude terms. The reconstruction of the amplitudes A is not exactly the same for the two states due to slightly different photo-absorption cross-sections. The φ terms shown in Fig. 4(e) present a slightly different behavior. Fig. 4(c) shows the first derivative of the phases for the two states considered separately. This term is defined as the difference between two consecutive reconstructed φ phases and is centered between the two considered harmonics orders. In this illustration, the

shape of the A-state is mainly due to the harmonics and the continuum-continuum phases since the molecular phase is assumed to be negligible in this energy region. The difference between the measurements are mainly due to differences in the derivatives of the phases of the dipole matrix elements describing the transitions to the X and A states. This provides the difference in ionization time delay between the two states. Ionization delays up to 50 attoseconds have been measured experimentally on the peak of the shape resonance around 30 eV (around the harmonic order 20), and positive delays are also observed at lower photon energies [11].

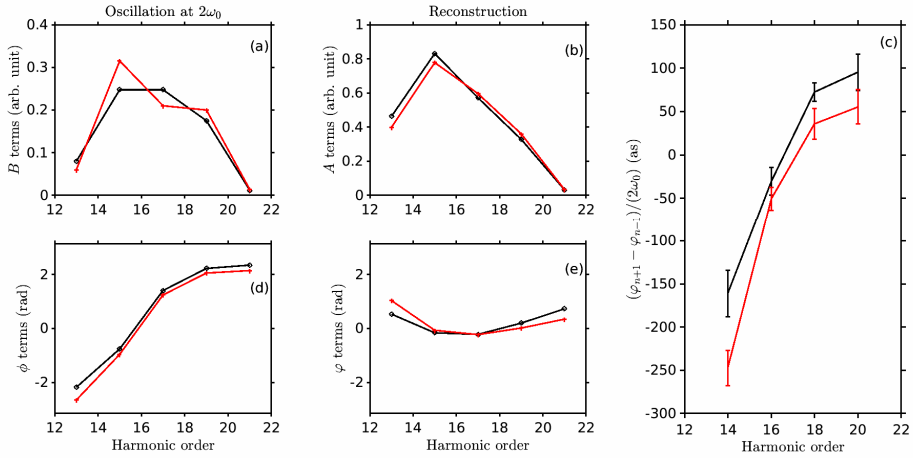


Fig. 4. Reconstruction of the ionization phase differences between the X and A-states of N_2^+ represented in black and red respectively. Measured amplitude B (a) and phase ϕ (d) of oscillation at $2\omega_0$. Reconstructed amplitude A (b) and phase ϕ (e) terms and (c) the corresponding phase derivative of the two states, considered separately, in attoseconds.

CONCLUSION

The HHG- $2\omega_0$ scheme is an alternative solution to the RABBIT method that provides the same attosecond information on the dynamics of a quantum system. However, the HHG- $2\omega_0$ and RABBIT methods have significant conceptual differences. The HHG- $2\omega_0$ method does not significantly change the photoelectron KES but relies on electron momentum β_{odd} asymmetry, while the RABBIT method duplicates the number of contributions that oscillate with the sidebands appearance described by β_{even} angular terms. In the HHG- $2\omega_0$ method, both the spectral amplitude and phase of the initial pulse has an influence on both the amplitude and the phase of the

oscillations. In RABBIT, only the system's phases play a role on the phases of the sideband oscillations. The HHG- $2\omega_0$ scheme provides a better contrast when using a harmonic comb that has a rapidly varying envelope and a non-flat phase, while RABBIT sidebands measurements exhibit a higher contrast. Let's notice that the analysis of the RABBIT oscillation measured over the harmonics peaks is conceptually close to the HHG- $2\omega_0$ method. The reconstruction of the HHG- $2\omega_0$ method involves both the amplitude and phase of the experimental oscillation. In both methods, the attosecond oscillations appear at twice the dressing field $2\omega_0$. Both methods allow us to reconstruct the temporal profile of an attosecond pulse train [13, 15] and measure the ionization time delay in atoms and molecules [11, 24, 27].

The present HHG- $2\omega_0$ method is however unique when photoionization proceeds through several open channels, which leads to spectral congestion in the usual RABBIT measurements due to many overlapping contributions. This is already the case for small molecules such as nitrogen [11] and atoms with a strong spin-orbit coupling such as Xenon, so that one can expect that the HHG- $2\omega_0$ method would be even more useful in complex molecules where the number of ionization channels is much larger. Also, it is of interest when both even and odd harmonics are generated and more generally, in all the configurations where only one attosecond pulse is present per optical cycle of the dressing field [14, 16, 28].

Nowadays, many RABBIT-like interferometric scheme appear to access the attosecond information under various experimental conditions. For example, using the free-electron-laser radiation, the harmonics are separated by $3\omega_0$ and the system can be dressed by one and two ω_0 photons [29]. The development of different interferometric configurations can extend the "toolbox" of attosecond science to get suitable experimental arrangements for the study of attosecond dynamics in a large variety of quantum systems.

ACKNOWLEDGMENTS

We acknowledge the support of CNRS, ANR-16-CE30-0012 "Circé", ANR-15-CE30-0001 "CIMBAAD" and the Fédération de recherche André Marie Ampère. EP, AP and FM are supported by the MINECO grant FIS2016-77889-R. FM acknowledges support from the "Severo Ochoa" Programme for Centres of Excellence in R&D (MINECO, Grant SEV-2016-0686) and the "Maria de Maeztu" Programme for Units of Excellence in R&D (MDM-2014-0377).

REFERENCES

1. M. J. J. Vrakking, F. Lépine, “Attosecond Molecular Dynamics”, The Royal Society of Chemistry, 2019.
2. D. Baykusheva, H. J. Wörner, “Attosecond Molecular Spectroscopy and Dynamics”, Elsevier, 2020, chapter 3.
3. U. Becker, D. A. Shirley, “VUV and Soft X-Ray Photoionization”, Plenum Press, New York, 1996.
4. R. Pazourek, S. Nagele, J. Burgdörfer, *Rev. Mod. Phys.*, **87**, 765 (2015).
5. P. M. Paul, *et al.*, *Science*, **292**, 1689 (2001).
6. M. Isinger, *et al.*, *Science*, **358**, 893 (2017).
7. V. Gruson, *et al.*, *Science*, **354**, 734 (2016).
8. M. Huppert, *et al.*, *Phys. Rev. Lett.*, **117**, 093001 (2016).
9. M. Kotur, *et al.*, *Nat. Commun.*, **7**, 10556 (2016).
10. I. Jordan, *et al.*, *J. Opt.*, **20**, 024013 (2018).
11. V. Loriot, *et al.*, *J. Phys.: Photonics*, **2**, 024003 (2020).
12. T. J. B. Eppink, D. H. Parker, *Rev. Sci. Instrum.*, **68**, 3477 (1997).
13. V. Loriot, *et al.*, *J. Opt.*, **19**, 114003 (2017).
14. G. Laurent, *et al.*, *Phys. Rev. Lett.*, **109**, 083001 (2012).
15. G. Laurent, *et al.*, *Opt. Express*, **21**, 16914 (2013).
16. C. Thaury, F. Quéré, *J. Phys. B*, **43**, 213001 (2010).
17. A. L’Huillier, Ph. Balcou, *Phys. Rev. Lett.*, **70**, 774 (1993).
18. P. B. Corkum, *Phys. Rev. Lett.*, **71**, 1994 (1993).
19. R. Lopez-Martens, *et al.*, *Phys. Rev. Lett.*, **94**, 033001 (2005).
20. R. N. Zare, “Angular momentum”, Wiley & Sons, Inc., New York, 1988
21. G. Laurent, *et al.*, *J. Phys. Conf. Ser.*, **488**, 012008 (2014).
22. Y. Mairesse, F. Quéré, *Phys. Rev. A*, **71**, 011401(R) (2005).
23. B.L. Henke, E.M. Gullikson, J.C. Davis, *At. Data Nucl. Data Tables*, **54**, 181-342 (1993).
24. S. Haessler, *et al.*, *Phys. Rev. A*, **80**, 011404(R) (2009).
25. R. R. Lucchese, K. Takatsuka, V. McKoy, *Phys. Rep.*, **131**, 147 (1986).
26. E. P. Wigner, *Phys. Rev.*, **98**, 145 (1955).
27. S. Nandi, *et al.*, *Sci. Adv.*, **6**, eaba7762 (2020).
28. J. Mauritsson, *et al.*, *Phys. Rev. Lett.*, **100**, 073003 (2008).
29. P. K. Maroju, *et al.*, *Nature*, **578**, 386 (2020).

EPR TESTING OF ORGANIC VERSUS CONVENTIONAL MUSACEAE FRUITS

D.M. PETRIȘOR^{1,*}, G. DAMIAN², S. SIMON^{1,2}

ABSTRACT In the present study, the EPR spectroscopy was used to evidence differences in fruits of organically and conventionally grown bananas belonging to musaceae family. If in the investigated samples would be detected specific changes related to paramagnetic resonant centers, these could be regarded as a spectroscopic fingerprint in the differentiation of the organic and conventional fruits and vegetables. The EPR spectra were recorded from freeze-dried shell and pulp samples. The main paramagnetic species (iron, manganese and native semiquinone free radical) delivered for the investigated samples slight different EPR signals. In this stage, the results obtained by EPR testing put in evidence sensible differences between the two classes of samples, and draw the attention on differences in EPR signals recorded from banana pulp and shell.

Keywords: *EPR spectroscopy; organic food; conventional food.*

INTRODUCTION

Organic versus conventional food is a large debate subject especially regarding the food safety [1]. Chemical fertilizers, pesticides, herbicides, and plant hormones are often applied in intensive agricultural areas to maintain high yields [2]. All these are expected to be excluded in the organic farming.

Organic foods are not necessarily better for the body than conventional foods in terms of vitamin and nutrient content, but for sure they are less exposed to pesticides and antibiotic-resistant bacteria.

¹ *Interdisciplinary Research Institute on Bio-Nano-Sciences, Babes-Bolyai University, 400271, Cluj-Napoca, Romania*

² *Faculty of Physics, Babes-Bolyai University, 400084, Cluj-Napoca, Romania*

* *Corresponding author: dinapetrisor@yahoo.co.uk*

According to a comprehensive review on human health implications of organic food and organic agriculture, the organic food may reduce the risk of allergic diseases and of overweight and obesity [3]. The organic foods, despite the higher production costs, are preferable. Consequently, scientific research on food quality and nutritional extracts is considered a high priority by several international organizations [4, 5]. The most analyzed categories of foods are fruits, organic and non-organic vegetables, cereals, meat, eggs and milk [6].

Bananas are the fourth most important food crop in the world after rice, maize and wheat [7]. They belong to the monocotyledonous family of musaceae. Demand and production of organic bananas have been growing in recent years, especially concerning that organic bananas contain no fat or cholesterol and are easy to digest as they are a good source of various nutrients such as vitamin B6, vitamin C, magnesium and potassium. Moreover, the consumption of organic bananas as part of the daily diet helps reduce the chances of stroke and heart attack as the fruit generally helps reduce cholesterol, improve blood sugar control, and enhance digestion. Furthermore, organic bananas contain iron, and thus can stimulate the production of hemoglobin in the blood [8]. But, the requirements of organic production in terms of soil quality, water management, climate change mitigation and biodiversity conservation, make that the organic banana supply to be naturally limited.

The interest in establishing the characteristics of conventionally grown and organically grown bananas is quite high, in the specialized literature there are different case studies. Comparative studies regarding fruit dimensions, color, local differences in surface pigmentation, weight and firmness shown that organically and conventionally grown product had almost identical qualities [8].

Electron Paramagnetic Resonance (EPR) spectroscopy can be used to characterize the changes concerning paramagnetic species present in foods. Depending on the types of biochemical processes involved in fruit or vegetables growth and maturation, these paramagnetic centers may or may not be present, and may have different shapes and intensities of EPR signals [9]. EPR method is often applied for food analysis, particularly in detection of Fe^{3+} , Mn^{2+} and Cu^{2+} metal ions with long relaxation times [10]. Transition metal ions are generally paramagnetic by virtue of their partially filled d orbitals. Using this spectroscopic method for the study of organic and conventional foods, some characteristic features for the studied samples can be established.

The present study aims to evidence by EPR analysis the spectroscopic differences between shell and pulp of banana fruits grown under organic and conventional conditions. Possible characteristic changes could be a spectroscopic fingerprint in the differentiation of organic and conventional fruits and vegetables.

EXPERIMENTAL

Conventionally and organically grown bananas originating in Peru, used in the present study, were purchased from the local market. In order to obtain the samples in powder form, both the shell and the pulp of the fruits were lyophilized by using an Alfa 1-2 LD Christ Freeze dryer, by keeping the samples in a controlled atmosphere (pression 0.04 ± 0.024 mbar and temperature $-50^\circ\text{C} \div -54^\circ\text{C}$), for 78 h. EPR measurements were performed on a Bruker EMX spectrometer operating in X-band (~ 9 GHz), with 100 kHz modulation frequency. The EPR spectra were recorded at room temperature, for similar amount of grinded samples.

RESULTS AND DISCUSSION

The EPR spectra of conventionally and organically grown bananas (liophilized shell and pulp) are shown in Figure 1. The six-line multiplet spectrum centered at $g = 2.0$ is a fingerprint of paramagnetic Mn^{2+} ions subjected to tetragonal crystal field and hyperfine magnetic interaction between unpaired electrons and nuclear spin ($I = 5/2$). The average hyperfine splitting between neighboring peaks of the Mn^{2+} sextet reflects, approximately, the degree of ionicity of the bonds involving the manganese ions, and, for an average hyperfine splitting of 80–90 G, is considered the ionicity degree of 80–90% and the covalency degree of 20–10% [11].

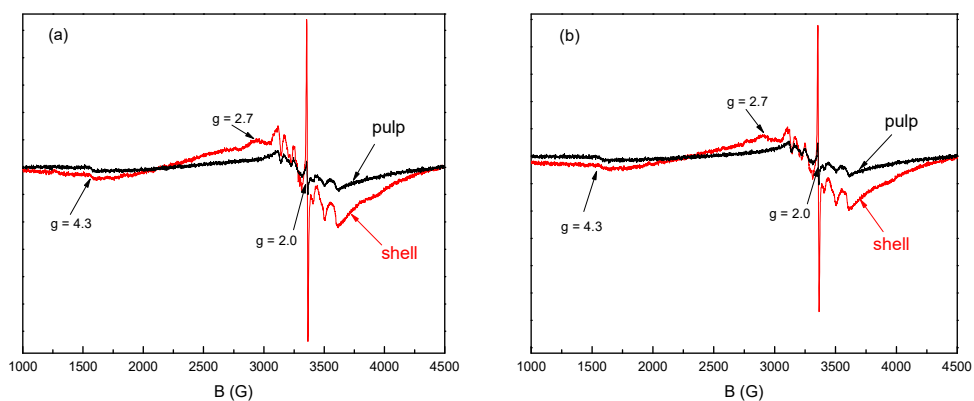


Fig. 1. EPR spectra of freeze-dried bananas: (a) conventional fruit; (b) organic fruit.

Manganese is a trace element present in almost all foods of vegetal origin, and manganese ions play an important role in biochemical processes especially in green plants, as cofactors of proteins and enzymes [10-13]. In the studied samples, the EPR intensity of the signals associated with Mn^{2+} ions are much higher in the shell of both conventional and organic fruits. In the hyperfine structure of Mn^{2+} EPR line no changes are observed, the average hyperfine splitting is kept 90 G in all samples.

At the same time, on the six-line multiplet spectrum a narrow signal of organic free radical can be observed at $g = 2.0$ (Fig. 1). This line is assigned to semiquinone radical [10, 12, 14, 15] and it was shown that Mn^{2+} ions play an important catalytic role in the formation of this organic free radical [12]. Semiquinones may be regarded as a special kind of phenoxyl radicals [16]. They result as free radicals after removal of a hydrogen atom by dehydrogenation of a hydroquinone. Quinones (Q) are used as oxidizing agents in organic synthesis, whereas hydroquinones (H_2Q) are used as reducing agents [17]. The reduction of a quinone can occur in two sequential one-electron transfer reactions (Eqs.1 and 3). The complete reduction of a quinone to a hydroquinone requires two electrons and two protons (Eq. 3). The intermediate semiquinone ($SQ^{\bullet-}$) is a relatively stable free radical, compared to highly reactive free radicals such as the hydroxyl radical; however, semiquinone radicals are relatively unstable species compared to quinones and hydroquinones [17].



Nevertheless, it was shown that semiquinones can have extremely long half-lives, up to days at 37 °C, and tend to be neither reactive nor toxic [18].

A weak broad shoulder around $g = 2.7$ is recorded only from shell samples (Fig. 1). This resonant signal is assigned to Mn^{2+} ions disposed in sites of distorted tetrahedral symmetry [12]. It was assumed that also the weak signal at $g = 4.3$ arises from Mn^{2+} ions in distorted tetrahedral symmetry [12, 15], but additional research on Mn^{2+} EPR spectra of vegetal samples [15] proved that this signal arises from Fe^{3+} ions. Fe^{3+} experiencing a rhombic ligand/crystal field / in a fully rhombic ligand field configuration. [11]. The low intensity of $g = 4.3$ signal arising from Fe^{3+} ions denotes a low amount of iron as trace element. Nevertheless, the iron concentration could be due several causes like iron concentration in the soil, specific absorption by the plant, or environmental conditions [19].

Resuming, the EPR spectra evidence Mn^{2+} and Fe^{3+} ions and semiquinone free radical. A significant difference between the intensity of organic free radical can be observed (Fig.1) for shell and pulp samples. Both for conventional and organic banana shell, the intensity of the semiquinone radical is higher than for pulp sample, probably because the shell is much more exposed to atmospheric oxygen than the pulp.

Considering as reference the same amplitude for Fe^{3+} EPR signal, one observes for conventionally grown sample that the amplitude of free radical line is about 10 times higher in shell than in pulp, while in organically grown sample this ratio is lower, namely about 7. As a result, according to this reference, for the samples investigated in this study, the shell appears to concentrate a relative larger number of free radicals than in pulp, in conventional and organic bananas. Total antioxidant capacity of organics is reported to exceed by 80% that of conventionally grown products [20]. For the samples investigated in this study, the shell appears to concentrate a relative larger number of free radicals in conventional than in organic bananas, while in pulp a higher number of free radicals is observed for organic bananas.

A careful examination of pulp (Fig. 2) and shell (Fig. 3) spectra highlights differences in the two classes of fruits regarding the amount of free radicals. Referencing the amplitude of the free radical signal to that of the Mn^{2+} hyperfine structured envelope line (Fig. 2), one obtain for conventional pulp sample the ratio 0.85 and for organic pulp sample this ratio is increased to 1.2.

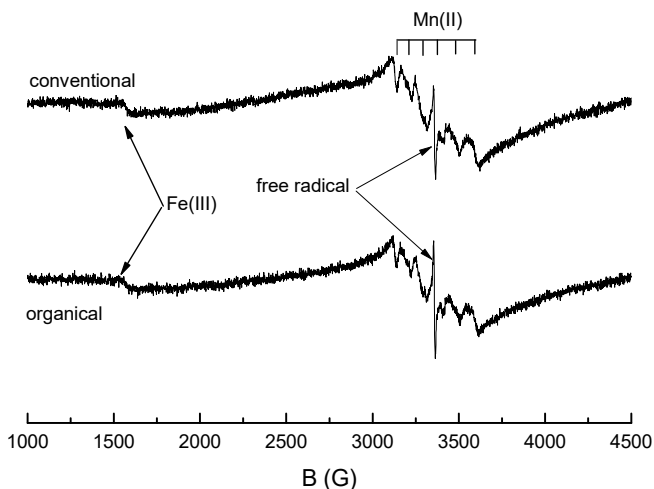


Fig. 2. EPR spectra of organic and conventional banana pulp.

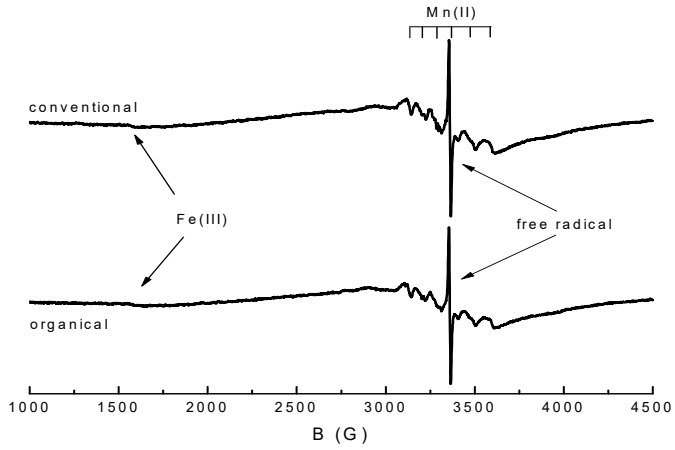


Fig. 3. EPR spectra of organic and conventional banana shell.

This is not the case in shells (Fig. 3) wherein a similar value about 3.4 is obtained for both organic and conventional samples as ratio between the amplitude of the free radical signal to that of the Mn^{2+} hyperfine structured envelope resonance line.

Concerning the free radical resonance line, it appears worth to analyze beside the relative line intensity also the peak-to-peak width in the organic and conventional samples (Fig. 4).

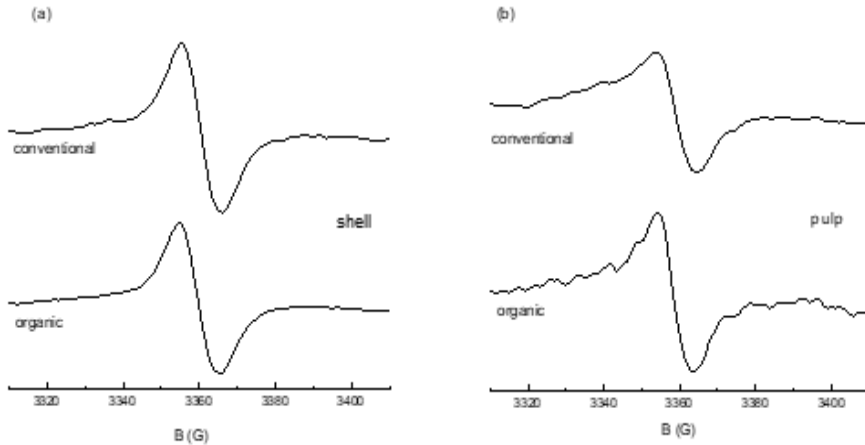


Fig. 4. EPR signal of semiquinone radicals in organic and conventional samples: (a) shell and (b) pulp.

The free radical line width in shells is the same, 11.2 G, both in organic and conventional samples, and the same value is also in pulp of conventional sample, but it is evidently lower, 9.1 G, in pulp of the organic sample. On the other hand, the line intensity is proportional to the number of semiquinone free radicals. Assuming the line intensity as the product between line height and square of peak-to-peak line width [21], one can conclude that the number of semiquinone free radicals is higher in pulps of organic than in pulps of conventional samples (Fig. 4b).

CONCLUSIONS

The present EPR study attempted to characterize EPR spectroscopic differences detectable in freeze-dried banana fruits grown under natural and conventional conditions, of same geographic origin. The analysis of room temperature EPR spectra points out some changes delivered by the resonant paramagnetic species Fe^{3+} , Mn^{2+} and semiquinone free radical, both in pulp and in shell of the fruits. Regardless of growth conditions, the Fe^{3+} ions occur in sites of rhombic crystal field; Mn^{2+} ions in pulp are subjected only to tetragonal crystal field and the line is split into sextet due to hyperfine interaction experienced by unpaired electrons with the nuclear spins, while in shell a low number of Mn^{2+} ions are detected also in sites of distorted tetrahedral symmetry; semiquinone free radicals occur in much higher number in shell than in pulp.

Specific differences between organic and conventional fruits refer to the ratio between the amplitude of the signals arising from free radicals in shell and pulp that is about 10 for conventionally grown and about 7 for organically grown fruits. The peak-to-peak width of free radical line width in pulp of conventional sample is 11.2 G, but this is diminished to 9.1 G in pulp of the organic sample. According to the intensity of EPR signal delivered by semiquinone free radicals, the number of these radicals is lower for shell and higher for pulp, in organically, than in conventionally grown samples. These results could promote further investigations concerning an EPR spectroscopic fingerprint in the differentiation of the organic and conventional musaceae fruits.

REFERENCES

1. J.M. Garcia and P. Teixeira, "Organic versus conventional food: A comparison regarding food safety", *Food Reviews International*, 33(4), 424-446, (2017).
2. G. Haas, F. Wetterich and U. Kopke, "Comparing intensive, extensified and organic grassland farming in southern Germany by process life cycle assessment", *Agriculture, Ecosystems and Environment*, 83, 43-53. (2001).
3. A. Mie et al., "Human health implications of organic food and organic agriculture: a comprehensive review", *Environmental Health*, 16(111), 1-22, (2017)

4. B. Burlingame and S. Dernini, "Sustainable diets and biodiversity, Directions and solutions for policy, research and action", Edited by B. Burlingame and S. Dernini, Nutrition and Consumer protection division FAO, (2012).
5. Sustainable Food Systems Programme, <http://www.unep.org/10yfp/programmes/sustainable-food-systems-programme>, (2016).
6. A. El-Bassel Hamdy and H. El-Gazzar Hany, "Comparable study between organic and nonorganic vegetables in their contents of some nutritive components", *Journal of Medicine in Scientific Research*, 2, 204-208, (2019).
7. A. Viljoen, K. Kunert, A. Kiggundu and J.V. Escalant, "Biotechnology for sustainable banana and plantain production in Africa: the South African contribution", *South African Journal of Botany*, 70(1), 67–74, (2004).
8. L.P. Caussiol and D.C. Joyce, "Characteristics of banana fruit from nearby organic versus conventional plantations: A case study", *The Journal of Horticultural Science and Biotechnology*, 79(5), 678-682, (2004).
9. I. Csillag and G. Damian, "EPR study of organically-grown versus greenhouse strawberries", *Studia UBB Physica*, 61 (LXI), 1, 21-26, (2016).
10. C. Drouza, S. Spanou and A.D. Keramidas, "EPR methods applied on food analysis", *IntechOpen, Topics from EPR research*, Chapter 4, 45-64, (2018).
11. Z. Klencsar and Z. Kontos, "EPR Analysis of Fe³⁺ and Mn²⁺ complexation sites in fulvic acid extracted from lignite", *The Journal of Physical Chemistry A*, 122, 3190–3203, (2018).
12. M. Polovka, V. Brezova and A. Stasko, "Antioxidant properties of tea investigated by EPR spectroscopy", *Biophysical Chemistry*, 106, 39–56, (2003).
13. S.H. Reaney, C.L. Kwik-Urbe and D.R. Smith, "Manganese oxidation state and its implications for toxicity", *Chemical Research in Toxicology*, 15, 1119-1126, (2002).
14. M.A. Morsy and M.M. Khaled, "Novel EPR characterization of the antioxidant activity of tea leaves", *Spectrochimica Acta Part A*, 58, 1271–1277, (2002).
15. R. Biyik and R. Tapramaz, "Transition metal ions in black tea: an electron paramagnetic resonance study", *Transition Metal Chemistry*, 35, 27–31, (2010).
16. K.-D. Asmus, M. Bonifačić, "Part I: Introduction to free radicals. Free radical chemistry", in *Handbook of Oxidants and Antioxidants in Exercise*, 1st Edition, Elsevier Science, (2000).
17. Y. Song and G.R. Buettner, "Thermodynamic and kinetic considerations for the reaction of semiquinone radicals to form superoxide and hydrogen peroxide", *Free Radical Biology & Medicine*, 49(6), 919-962, (2010).
18. J.P. Kehrer, J.D. Robertson and C.V. Smith, "Free Radicals and Reactive Oxygen Species", In: McQueen CA (Ed), *Comprehensive Toxicology*, Elsevier, Oxford, Second Edition, 277-307, (2010).
19. W. M. Stewart, D. W. Dibb, A. E. Johnston and T. J. Smyth, "The Contribution of Commercial Fertilizer Nutrients to Food Production", *Agronomy Journal*, 97(1), 1-6, (2005).
20. R. Bernacchia, R. Preti and G. Vinci, "Organic and conventional foods: differences in nutrients", *Italian Journal of Food Science*, 28 (4), 565-578, (2016).
21. D.T. Burns and B.D. Flockhart, "Application of the quantitative EPR", *Philosophical Transactions of the Royal Society A*, 333, 37-48, (1990).

TUNNELING IONIZATION STUDY OF LINEAR MOLECULES IN STRONG-FIELD LASER PULSES*

V. PETROVIĆ¹, H. DELIBAŠIĆ^{1,**}, I. PETROVIĆ²

ABSTRACT We theoretically studied photoionization of atoms and molecules in the frame of Perelomov-Popov-Terent'ev (PPT) and Ammosov-Delone-Krainov (ADK) theories. Strong-field single ionization of two diatomic molecules, N_2 and O_2 , are studied and compared to Ar and Xe atoms, using an 800 nm Ti:sapphire laser in the 3×10^{13} to 1×10^{15} Wcm^{-2} intensity range. To eliminate disagreement between theoretical and experimental findings in a low intensity fields ($\sim 6 \times 10^{13}$ Wcm^{-2}), we considered the influence of shifted ionization potential. Including these effects in the ionization rates, we numerically solved rate equations in order to determine an expression for the ionization yields. The use of modified ionization potential showed that the ionization yields will actually decrease below values predicted by original (uncorrected) formulas. This paper will discuss the causes of this discrepancy.

Keywords: tunneling ionization, ionization rate, ionization yield, molecules.

INTRODUCTION

In the past decade substantial progress has been made in the understanding of the dynamics of molecules in intense-laser fields (10^{13} – 10^{18} Wcm^{-2}) [1,2]. As a result, experimental, theoretical and computational investigation of this phenomena have demonstrated fundamental processes such as bond softening and hardening, laser induced alignment, and enhanced ionization at critical internuclear distances. Most of these phenomena are based on tunnel ionization of neutral atoms and molecules as the first step of the physical processes [3].

* Presented at the First Annual Workshop for the COST Action Attosecond Chemistry (ATTOCHEM) CA18222, organized on-line, September 9-11, 2020.

¹ Faculty of Science, University of Kragujevac, Radoja Domanovića 12, Kragujevac, Serbia.

² Technical Collage of Applied Studies, University of Kragujevac, Kragujevac, Serbia.

** Corresponding author: hristinadelibasic@gmail.com

There is a wealth of theoretical approaches to the atomic photoionization dynamics in a strong field, which can be defined as tunnel, multiphoton, or some combination of both. Keldysh [4] was first who introduced well known parameter to distinguish tunnel and multiphoton photoionization process, $\gamma = \omega\sqrt{2I_p}/F$, where I_p is unperturbed ionization potential, F the amplitude of the electric field and ω the laser frequency. It was widely accepted that for $\gamma \gg 1$ multiphoton ionization is the dominant process, while for $\gamma \ll 1$ tunnel. It is worth noting that according to Reiss [5], the regime when $\gamma \sim 1$ at $\lambda = 800$ nm ionization in a strong laser field can successfully be described as a tunneling process. Here and throughout the paper, all equations are given in atomic units ($e = m_e = \hbar = 1$) [6] unless otherwise stated.

Keldysh theory is extended into the so-called Strong Field Approximation (SFA) [7]. Following the Keldysh formalism of the tunneling ionization rate in a strong electromagnetic field Perelomov, Popov and Terent'ev developed another tunneling model (PPT) [8] that was further extended by Ammosov, Delone and Krainov and is now known as ADK-theory [9]. During the last years, the scope of strong field physics has been extended to the systems more complex than atoms, including molecules, fullerenes and clusters where all abovementioned theories are also being suitably adapted (molecular orbital SFA (MO-SFA) [10], molecular orbital PPT (MO-PPT) [11], and molecular orbital ADK (MO-ADK) [12]). All mentioned theories are based on single active electron approximation (SAE) where only the one electron interacts with the applied laser field. Also, experimental results [13,14] show excellent agreement with these one theoretically predicted by the commonly used ADK, as well MO-ADK in the case of noble gasses and small molecules. Because of additional nuclear degrees of freedom, the motion of electrons and nuclei (there are nuclear rotational and vibrational dynamics) which must be taken into consideration, molecules are much more complex to model theoretically than atoms. Models are still being developed and in generally they are more complex than earlier [15,16].

THEORETICAL FRAMEWORK

The abovementioned atomic tunneling theories [7-12] have been very successful in describing the ionization rates of both atoms and molecules. It is well known that these theories depend primarily on the field intensity, I (relationship between intensity (I) and electric field amplitude (F), is given by: $F \sim \sqrt{I}$), and ionization potential, I_p . If the ionization potential is one of the most important

quantities, one would expect similar ionization rates for molecules and atoms with similar ionization potentials, the so-called companion atoms. Several experiments were performed in order to measure the ratio of ion yields of diatomic molecules and their companion atoms [17,18]. The findings have revealed that some molecules are harder to ionize than their companion atoms. This phenomenon is known as suppressed ionization [19].

In this paper we have aim to explore how corrections on the ionization potential, I_p , influence the ionization rate, $W(F, t)$, of homonuclear diatomic molecules, N_2 and O_2 , and their companion atoms Ar and Xe , respectively. As Table 1 illustrates, these atoms and molecules have comparable ionization potentials. To achieve this, we modified I_p by taking into account the Stark shift, I_{st} , and the ponderomotive potential, U_p .

Table 1. Ionization potentials of diatomic molecules, N_2 and O_2 , and companion atoms, Ar and Xe [20].

	Ar	N_2	Xe	O_2
I_p [atomic units]	0.57916	0.57255	0.45202	0.44319

If a quantum system is found in a state with energy I_p and is perturbed by an external monochromatic field of amplitude F and frequency ω , then the shift of the ionization energy is well known as a Stark shift which can determined by the following expression: $I_{st} = \alpha_p F^2/4 + \gamma_h F^4/24$ [21]. In this inline equation, α_p represents the dipole polarizability, while γ_h is the dipole hyperpolarizability. In addition, this field also causes the oscillating movement of electron. The ponderomotive potential, i.e. the average oscillation kinetic energy of a free electron in the electric field of the laser with strength F , is then readily calculated as $U_p = F^2/4\omega^2$ [22]. Having both effects in mind, we can write the corrected ionization potential I_p^{corr} in the following form:

$$I_p^{corr} = I_p + I_{st} + U_p = I_p + \frac{\alpha_p F^2}{4} + \frac{\gamma_h F^4}{24} + \frac{F^2}{4\omega^2}. \quad (1)$$

The values of polarizability α_p and hyperpolarizability γ_h for different linear molecules can be found in [21].

In the following we briefly review the basic rate equations of the MO-ADK and the MO-PPT theories.

MO-ADK ionization rate

The MO-ADK theory is extension of the ADK tunneling theory on the more complex system, molecules. Following exactly the same procedure as in [12], the tunneling ionization rate of linear molecules, W_{MOADK} , can be calculated as [12]:

$$W_{\text{MOADK}} = \frac{B^2(m)}{2^{|m|}|m|!} \frac{1}{\kappa^{\frac{2Z_C}{\kappa}-1}} \left(\frac{2\kappa^3}{F}\right)^{2Z_C/\kappa-|m|-1} \text{Exp}\left[-\frac{2\kappa^3}{3F}\right], \quad (2)$$

where m is the magnetic quantum number along the molecular axis, Z_C is the effective Coulomb charge [23], κ is the characteristic momentum of the bound state, $\kappa = \sqrt{2I_p}$, and I_p is already defined and here presents ionization potential for the given valence orbital. The factor $B^2(m)$ in Eq. (2) measures the electron density in the tunneling region along the direction of the electric field and for the case of linear molecules can be expressed as: $B(m) = \sum_l C_l Q(l, m)$, where C_l is the structure coefficient of the molecule, l is the angular momentum quantum number and $Q(l, m)$ is the coefficient given by: $Q(l, m) = (-1)^m [(2l+1)(l+|m|)!]/(2(l-|m|)!)]^{1/2}$. The values of C_l for a specific linear molecule can be found in [12].

MO-PPT ionization rate

Based on PPT theory [8] and results presented by Tong et al. [12], Benis and his coworkers in [11] improved Eq. (1), developing the MO-PPT model. Based on this model, the ionization rate of linear molecules is given by [11]:

$$W_{\text{MOPPT}} = \frac{B^2(m)}{2^{|m|}|m|!} \frac{A_m(\omega, \gamma)}{\kappa^{2Z_C/\kappa-1}} \left(\frac{2\kappa^3}{F(1+\gamma^2)}\right)^{2Z_C/\kappa-|m|-1} \times \text{Exp}\left[-\left(\frac{2\kappa^3}{3F}\right)g(\gamma)\right]. \quad (3)$$

It is worth noting that the MO-ADK model is a simplified version of MO-PPT. When Keldysh parameter, $\gamma \rightarrow 0$, the Eq. (3) goes back to the MO-ADK rate (Eq. (2)). Regard to MO-ADK, Eq. (4) has the following two correction factors $A_m(\omega, \gamma)$ and $g(\gamma)$ [24], which for the case of the tunneling ionization can be defined as: $A_m(\omega, \gamma) = \frac{4\gamma^2}{(1+\gamma^2)\sqrt{3\pi}|m|!} \sum_{k \geq \nu}^{\infty} \text{Exp}[-\alpha(k' - \nu)] w_m(\sqrt{\beta(k' - \nu)})$ and $g(\gamma) = 1 - \frac{1}{10}\gamma^2 + \frac{9}{280}\gamma^4$ [12]. In the above equations the following

coefficients are introduced [24]: $\alpha(k - \nu) = 2(k - \nu)^3/3$, $\beta(k - \nu) = 2(k - \nu)/\sqrt{1 + \gamma^2}$, $\nu = I_p \left(1 + \frac{1}{2\gamma^2}\right)/\omega$, $k' = \left\langle \frac{I_p}{\omega} + 1 \right\rangle$ and $w_m(\sqrt{\beta(k - \nu)}) = \frac{(\sqrt{\beta(k - \nu)})^{2|m|+1}}{2} \int_0^1 \frac{\text{Exp}[-t\sqrt{\beta(k - \nu)}]t^m}{\sqrt{1-t}} dt$. The symbol $\langle \rangle$ indicates the integer part of the value inside, which refers to the minimum number of photons required to ionize the system.

Corrections of MO-ADK and MO-PPT ionization rates

To analyze how the ionization rates W_{MOADK} and W_{MOPPT} are affected by the corrected ionization potential I_p^{corr} , we substituted the unperturbed ionization potential I_p with the shifted one, I_p^{corr} , in the MO-ADK and MO-PPT rate equations. We assume the envelope of the electric field to be a Gaussian beam, $F_G(t) = F_0 \exp[-4t^2/\tau^2]$ (τ is full width at half maximum (FWHM) of the laser pulse), in our calculations. The modulation of generally assumed laser beam shape, F , with the Gaussian shaped laser beam, $F_G(t)$, allows us to compare our results with the experimental data [25].

First, we incorporated the Gaussian laser beam shape, $F_G(t)$, and corrected ionization potential, I_p^{corr} , in the formula for the MO-ADK ionization rate, W_{MOADK} , and obtained the following expression:

$$W_{\text{MOADK}}^{\text{corr}}(t) = \frac{B^2(m)}{2^{|m|}|m|!} \frac{1}{\sqrt{2I_p^{\text{corr}}(t)}^{2Z_C/\sqrt{2I_p^{\text{corr}}(t)}-1}} \left(\frac{2(2I_p^{\text{corr}}(t))^{3/2}}{F_G(t)} \right)^{2Z_C/\sqrt{2I_p^{\text{corr}}(t)}-|m|-1} \times \text{Exp} \left[-\frac{2(2I_p^{\text{corr}}(t))^{3/2}}{3F_G(t)} \right]. \quad (4)$$

We repeated the same procedure in order to obtain the corrected version of the standard MO-PPT ionization rate, using Eq. (3):

$$W_{\text{MOPPT}}^{\text{corr}}(t) = \frac{B^2(m)}{2^{|m|}|m|!} \frac{A_m^{\text{corr}}(\omega, \gamma^c(t))}{\sqrt{2I_p^{\text{corr}}(t)}^{2Z_C/\sqrt{2I_p^{\text{corr}}(t)}-1}} \times \left(\frac{2(2I_p^{\text{corr}}(t))^{3/2}}{F_G(t)(1+(\gamma^c(t))^2)} \right)^{2Z_C/\sqrt{2I_p^{\text{corr}}(t)}-|m|-1} \text{Exp} \left[-\left(\frac{2(2I_p^{\text{corr}}(t))^{3/2}}{3F_G(t)} \right) g(\gamma^c(t)) \right]. \quad (5)$$

For the sake of optimizing Eq. (5), we introduced the corrected Keldysh parameter, $\gamma^c(t)$, in the following form: $\gamma^c(t) = \omega\sqrt{2I_p^{corr}(t)}/F_G(t)$.

RESULTS AND DISCUSSION

In this section results of a theoretical investigation of the modified ionization rates, $W_{MOADK}^{corr}(t)$ and $W_{MOPPT}^{corr}(t)$, have been presented and compared with experimental results (taken from [25]). We considered the case of single ionized diatomic molecules, N_2 and O_2 , and noble atoms, Ar and Xe , which are the most commonly used targets in strong-field studies. This was accomplished by considering a $\lambda = 800$ nm, central wavelength pulse with a 20 – 30 fs duration. Field intensities, I , have been varied within the range: $I = 3 \times 10^{13} - 1 \times 10^{15} \text{ Wcm}^{-2}$. These parameters limited the value of the Keldysh parameter in the range which is characteristic for the tunnel ionization. We assumed the Gaussian beam profile with, step by step, included fully corrected ionization potential. The yields presented in this paper are normalized to the maximum value which is $\sim 1.237 \times 10^9$, while the rates are normalized at the saturation intensity, so that the maximum yield denotes $W_{max} = 1$ and $\log_{10}(W_{max}) = 0$.

In Fig.1 we presented comparative review of the rates for O_2 molecule, obtained by the $W_{MOADK}(t)$ and the $W_{MOPPT}(t)$, as well as by the $W_{MOADK}^{corr}(t)$ and the $W_{MOPPT}^{corr}(t)$. It is obvious that the rates are underestimated in the MO-ADK compared with those from the MO-PPT until the field intensities $I < 6 \times 10^{13} \text{ Wcm}^{-2}$. This completely follows the findings in [13,26]. For the higher filed intensities, the $W_{MOADK}(t)$ overestimates the $W_{MOPPT}(t)$. Also, from Fig. 1 is obvious that the inclusion of both, the ponderomotive and the Stark shift, in the ionization potential causes the rate decrease. Graph shows cumulative decrease causes by both effects. This follows observed behavior in atom's systems [27]. Similar conclusions can be drawn for N_2 molecule when field intensity varies in the range $I = 2 \times 10^{13} - 2 \times 10^{14} \text{ Wcm}^{-2}$. It is important to note that the rates presented in Fig. 1 are very sensitive to the ponderomotive potential change. Under the same conditions, the Stark shift has a significantly smaller influence. Such result is completely in accordance with the theoretical predictions [9,10].

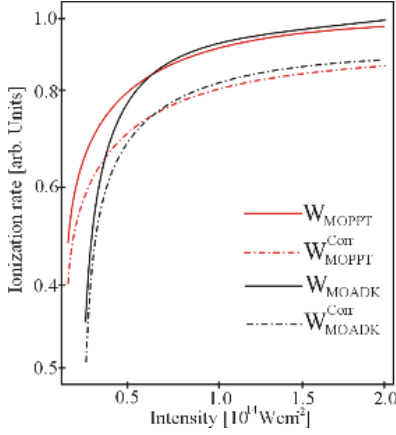


Figure 1. Comparative review of the ionization rates for O_2 molecule as a function of the laser intensity. The following notation is used: solid line for uncorrected ionization potential, I_p , and dot-dashed for fully corrected ionization potential, I_p^{corr} . Field intensity varies in the range $I = 2 \times 10^{13} - 2 \times 10^{14} \text{ Wcm}^{-2}$. Red lines are from the corrected MO-PPT and black from the MO-ADK model.

As we already mentioned, there are molecules with similar or almost same ionization potential with atoms. In this case, one can expect the similar ionization rates for molecule and its so-called companion atom, such as N_2 molecule and Ar atom or O_2 molecule and Xe atom. Many papers deal with this phenomenon [17,28,29]. Because of the similar ionization potential, one can expect similar ionization rate. In Table 2, the quantitative measure of the match is expressed through the ratio between belonging rates $N_2: Ar$ and $O_2: Xe$. Results are given for the assumed general form of laser beam shape. Our analysis clearly indicated that inclusion of the Gauss form of beam with the temporal evolution without spatial one, increases this ratio out of expected values.

Table 2. Ratios of single-ionization rates $W_{MOADK}^{corr,N_2}: W_{ADK}^{corr,Ar}$ and $W_{MOADK}^{N_2}: W_{ADK}^{Ar}$ for N_2 molecule with its companion Ar atom and $W_{MOADK}^{corr,O_2}: W_{ADK}^{corr,Xe}$ and $W_{MOADK}^{O_2}: W_{ADK}^{Xe}$ for O_2 molecule with its companion Xe atom. The ionization rate for ADK, W_{ADK} , is obtained by Eq. (1) of [9].

	$I [10^{13} \text{ Wcm}^{-2}]$				
	5	8	11	14	17
$W_{MOADK}^{N_2}: W_{ADK}^{Ar}$	1.31	1.18	1.10	1.06	1.02
$W_{MOADK}^{corr,N_2}: W_{ADK}^{corr,Ar}$	0.26	0.17	0.08	0.05	0.03
$W_{MOADK}^{O_2}: W_{ADK}^{Xe}$	0.029	0.018	0.010	0.005	0.001
$W_{MOADK}^{corr,O_2}: W_{ADK}^{corr,Xe}$	0.0058	0.0036	0.0019	0.0009	0.0001

From Table 2 one can observe that there is a significant difference between ratios for the same fixed laser field values, with and without included ionization potential's corrections. The corrective effects on the ionization potential suppress the ratio by a factor approximately five for the lower field intensities, with the intent to grow up with field increasing. In papers, it can be found significantly different results for N_2 and O_2 molecules and their companion atoms Ar and Xe . Tong et al. [12] suggested that if the N_2 molecule is aligned along the field direction, its ionization rate would be identical to Ar , and the ratio should be near 1, and for $I \sim 10^{14} \text{ Wcm}^{-2}$ ratio was calculated to be 0.98. In contrary, Liang et al. [30] suggested lower value, 0.2, or 0.7 by [31], and our results are in good agreement with them for the lower fields. Suppressed ionization ratio of O_2 molecule and Xe atom has been observed numerous of times [18,32]. Our results are in accordance with these findings. Kjeldsen and his group [17] predicted strongest suppression with the ratio below 0.01. In addition, their results clearly indicated that at lower intensities $I < 5 \times 10^{13} \text{ Wcm}^{-2}$, the experimental ratios are scattered between 0.02 and 0.2. The reason for disagreement between experimental and our result can be found in the fact that the experimentally obtained yield is always larger than those obtained by using theoretical models. That is why Hoang et al. [33] corrected the standard MO-ADK theory including the influence of permanent dipole and dynamic core-electron polarization on tunneling ionization. Such correction provided overall fairly good agreements with numerical solutions of the time-dependent Schrodinger equation, although a satisfactory agreement with experimental data in a wide laser intensity range was not achieved.

Next, we compared the theoretically predicted yields of molecule N_2 and its companion atom Ar , from the MO-ADK [12] and ADK [9] theory respectively, with experimental results. In order to achieve this, we integrated observed rates by the following expression [34]:

$$Y(t) = \int W(t)dt. \quad (6)$$

Mentioned comparison directly reveals the role of the electronic structure played in the tunneling ionization of molecules. According to [35] molecular ionization is known to depend on the structure and electron density of a molecule. Concretely, [36] found that the electronic structure influenced the ionization mechanisms for O_2 and F_2 molecules. Based on obtained results, they concluded that such trend can be expected for the other diatomic molecules. Earlier [37] stated the same for N_2 . The suppression of transition rate intensity of N_2 compared to Ar is in accordance with [12] where it can be found that the tunneling ionization rate is determined by

the suppressed barrier that occurs at a large distance from the atom and that the binding energy determines the tunneling rate each time the electron reaches the barrier. To obtain yield, we applied Eq. (6) on the molecule rate equations, Eqs. (2) and (4), and atom rate equation (Eq. (1)) from [9] over some definite time.

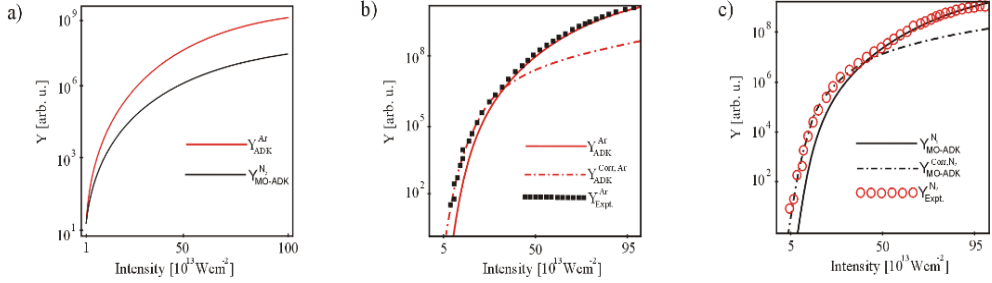


Figure 2. Yield as a function of laser field intensity. In all panels, the pulse duration is 30 fs and the laser wavelength is at 800 nm. We used the ADK and MO-ADK theory. The experimental data are from [25]. For all graphs the following notation is used: red line for Ar atom, black line for N_2 molecule. Experimental results are shown as black squares for Ar atom and as red open circles for N_2 molecule.

In Fig. 2(a), we compared the ionization yields of Ar atom and N_2 molecule, using the ADK [9] and the MO-ADK theory, without correction of ionization potential and with assumed Gauss laser beam shape. For intensities higher than $I \sim 5 \times 10^{13} \text{ Wcm}^{-2}$, the yields show difference in spite of the similar ionization potential between them. The ionization yield of N_2 is, about two order of magnitude suppressed, in comparison with Ar. This is in accordance with [17] and the fact that the ionization potential of Ar has a slightly higher ionization potential and the corresponding yield lies at bit higher. Next, in Fig. 2, panels (b) and (c), we presented the yields for Ar atom and N_2 molecule, obtained by using Eqs. (2) and (4) and compared them with experimental results taken from [25]. In both graphs, our yield signals, $Y_{\text{ADK}}^{\text{corr, Ar}}$ and $Y_{\text{MO-ADK}}^{\text{corr, N}_2}$, fit the experimental perfect in the lower range of field intensity. After the saturation intensity close to $I \sim 2 \times 10^{15} \text{ Wcm}^{-2}$ the corrected yields decrease much faster than measured. Such behaviour is expected since Guo's group in [25] stated that experimental conditions are chosen so that Stark shift and ponderomotive potential are strongly diminished. This fact could explain the discrepancy between experimental and theoretical results at higher field intensities presented in Figs. 2(a) and 2(b).

Finally, in Fig. 3, we analyzed the laser intensity dependent ionization rate, $W_{\text{MOPPT}}^{\text{corr}}(t)$, of the N_2 molecule at four different laser central wavelengths of $\lambda = (600, 800, 1000, 1200)$ nm. We would like to mention that the standard MO-ADK theory fails to give the wavelength dependence of ionization rates.

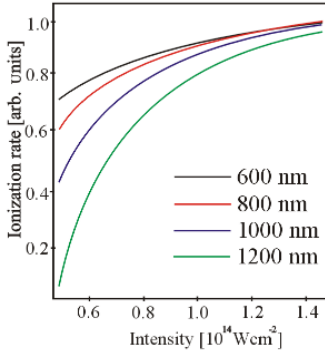


Figure 3. Comparison of the ionization rates predicted by the MO-PPT model of molecule N_2 as a function of laser field intensity at four different central wavelengths, λ , of: (black line) 600 nm, (red line) 800 nm, (blue line) 1000 nm and (green line) 1200 nm. The laser field is taken to be a Gaussian pulse with a pulse duration (full width at half maximum) of $\tau = 20$ fs.

From Fig. 3 one can observe that the increase of laser intensity leads to a logarithmic-like growth in the ionization rate for each value of wavelength. Our observations follow a similar trend to those reported by Zhao et al. [13,14]. Additionally, it is obvious that for lower wavelengths the ionization rates are more sensitive to changes in laser intensity. After $\sim 1.2 \times 10^{14} \text{ Wcm}^{-2}$ a saturation behaviour is observed up to the end of the laser pulse for the four curves. The results of experiments presented in [13] confirm this statement.

CONCLUSIONS

In conclusion, we have analyzed the influence of the ionization potential correction on the tunneling ionization rate for diatomic molecular system. Comparisons are made among the different versions of strong-field approximation. Our results clearly indicated that the correction of ionization potential effects the rate, by decreasing it. Also, some results show that the beam shape significantly influences the observed quantities.

ACKNOWLEDGMENTS

Authors are grateful to the COST Action CA18222 “Attosecond Chemistry” and the Serbian Ministry of Education, Science and Technological Development for financial support through Agreement No. 451-03-68/2020-14/200122.

REFERENCES

1. M. Magrakvelidze, C.M. Aikens, and U. Thumm, *Physical Review A* **86**(2) (2012) p.023402
2. P. Wang, C. Wu, M. Lei, B. Dai, H. Yang, H. Jiang, and Q. Gong, *Physical Review A* **92**(6) (2015) p.063412
3. T. Otobe, K. Yabana, and J.I. Iwata, *Physical Review A* **69**(5) (2004) p.053404
4. L. V. Keldysh, *Sov. Phys. JETP* **20**(5) (1965) p.1307
5. H.R. Reiss, *Phys. Rev. Lett.* **101** (2008) p.043002
6. R. McWeeny, *Nature* **243** (1973) p.196
7. H.R. Reiss, *Progress in Quantum electronics* **16**(1) (1992) p.1--71
8. A.M. Perelomov, V.S. Popov, and M.V. Terent'ev, *Sov. Phys. JETP* **23**(5) (1966) p.924
9. M.V. Ammosov, N.B. Delone, and V.P. Krainov, *In High intensity laser processes, International Society for Optics and Photonics* **664** (1986) p.138
10. W. Becker, J. Chen, S.G. Chen, and D.B. Milošević, *Physical Review A* **76**(3), (2007) p.033403
11. E.P. Benis, J.F. Xia, X.M. Tong, M. Faheem, M. Zamkov, B. Shan, P. Richard, and Z. Chang, *Physical Review A* **70**(2) (2004) p.025401
12. X.M. Tong, Z.X. Zhao, and C.D. Lin, *Physical Review A* **66**(3) (2002) p.033402.
13. S.F. Zhao, L. Liu, and X.X. Zhou, *Optics Communications* **313** (2014) p.74--79.
14. S.F. Zhao, J.K. Li, G.L. Wang, P.C. Li, and X.X. Zhou, *Communications in Theoretical Physics* **67**(3) (2017) p.289
15. P.K. Samygin, T. Morishita, and O.I. Tolstikhin, *Physical Review A* **98**(3) (2018) p.033401
16. M.M. Liu, M. Li, C. Wu, Q. Gong, A. Staudte, and Y. Liu, *Physical review letters* **116**(16) (2016) p.163004
17. T.K. Kjeldsen, and L.B. Madsen, *Physical Review A* **71**(2) (2005) p.023411
18. Z. Lin, X. Jia, C. Wang, Z. Hu, H. Kang, W. Quan, X. Lai, X. Liu, J. Chen, B. Zeng, and W. Chu, *Physical review letters* **108**(22) (2012) p.223001
19. J. Muth-Böhm, A. Becker, and F.H.M., Faisal, *Physical review letters* **85**(11) (2000) p.2280.
20. L.S. Cederbaum, *Theoretica chimica acta* **31**(3) (1973) p.239-260.
21. M. George, *Atoms, Molecules and Clusters in Electric Fields: Theoretical Approaches to the calculation of electric polarizability*, World Scientific (2006) p.503
22. G.G. Paulus, F. Zacher, H. Walther, A. Lohr, W. Becker and M. Kleber, *Phys. Rev. Lett* **80** (1998) p.484
23. J.L. Lebowitz, *Physical Review A* **27**(3) (1983) p.1491
24. F.A. Ilkov, J.E. Decker, and S.L. Chin, *Journal of Physics B: Atomic, Molecular and Optical Physics* **25**(19) (1992) p.4005
25. C. Guo, M. Li, J.P. Nibarger, and G.N. Gibson, *Physical Review A* **58**(6) (1998) p.R4271
26. S.F. Zhao, A.T. Le, C. Jin, X. Wang, and C.D. Lin, *Physical Review A* **93**(2) (2016) p.023413
27. H. Delibašić, and V. Petrović, *Chinese Physics B* **28**(8) (2019) p.083201

28. F. Grasbon, G.G. Paulus, S.L. Chin, H. Walther, J. Muth-Böhm, A. Becker, and F.H. Faisal, *Physical Review A* **63**(4) (2001) p.041402
29. S.F. Zhao, C. Jin, A.T. Le, and C.D. Lin, *Physical Review A* **82**(3) (2010) p.035402.
30. Y. Liang, A. Talebpour, C.Y. Chien, S. Augst, and S.L. Chin, *Journal of Physics B: Atomic, Molecular and Optical Physics* **30**(5) (1997) p.1369
31. Y.Z. Zhang, and Y.H. Jiang, *Advances of Atoms and Molecules in Strong Laser Fields: Imaging Ultra-fast Molecular Dynamics in Free Electron Laser Field* (2015).
32. B. Shan, X.M. Tong, Z. Zhao, Z. Chang, and C.D. Lin, *Physical Review A* **66**(6) (2002) p.061401.
33. V.H. Hoang, S.F. Zhao, V.H. Le and A.T. Le, *Physical Review A* **95**(2) (2017) p.023407.
34. E. Hasović, M. Busuladžić, A. Gazibegović-Busuladžić, D.B. Milošević and W. Becker, *Laser Phys.* **17** (2007) p.376.
35. M. Kotur, *Strong-field Dissociative Ionization as a Probe of Molecular Dynamics and Structure* (Doctoral dissertation, The Graduate School, Stony Brook University: Stony Brook, NY.), (2012).
36. D.A. Telnov and S.I. Chu, *Physical Review A* **79**(4) (2009) p.041401.
37. X. Chu and S.I. Chu, *Physical Review A* **70**(6) (2004) p.061402.

P2P (BILATERAL) COMMUNICATION BETWEEN NODEMCU ESP8266 BOARDS USING ARDUINO IDE

M. TODICA^{1,*}

ABSTRACT. Bilateral communication between the boards NodeMcu ESP826 is achieved using the WI FI capabilities of these devices and particularly code based on Arduino IDE. The system is used to control servos, DC motors or led. The duplex communication allows feedback action between sender and receiver. Real time feedback is obtained by particularly connection of the servo to the board.

Keywords: *Bilateral communication, NodeMcu ESP8266, Arduino.*

INTRODUCTION

The bilateral communication between two devices is now one of the most important features of the intelligent devices. The duplex communication is required especially in the long range remote control in order to ensure the feedback, the acknowledgement of the achievement of the transmitted order, [1, 2]. Generally two or many devices are connected to a router, which offer the possibility of connection between them trough a local network or trough the web. The system implies the use of an intermediate device, the router, and customized protocols. Sometimes, for short range of communication, we need a simple and direct communication between the devices, the so called peer to peer connection, (P 2 P). The intermediate device, the router, in not more necessarily and the communication is much faster. It is possible to achieve this task with simple equipment and popular software platforms as Arduino, [3]. One of the most popular devices able to fulfill this task is the NodeMcu ESP 8266 board. It is known especially for its capability to connect wirelessly to a local router (the internet), in the 2.4 GHz band, but with particular setting these boards can establish bilateral communication between them

¹ "Babes-Bolyai" University, Faculty of Physics, M. Kogalniceanu No 1, 400084 Cluj-Napoca, Romania.
* Corresponding author: mihai.todica@phys.ubbcluj.ro

without any intermediate devices. Two or many devices can be connected together, but the communication can be established only between the desired ones, using the identification MAC address of each board. In this work we will show how to establish bilateral communication between two NodeMcu ESP 8266 boards to control DC, servos or led with feedback control.

EXPERIMENTAL

The system consists of two parts, the sender, (the Master), named Tx, and the receiver, (the Slave), named Rx. The system is conceived to control 4 led or two DC motors and one servo SG 90. The led or the DC motors are controlled by four push switches connected between the pins D3, D4, D5, D6 and GND. The servo is controlled by one 10K potentiometer connected at +3.3V, GND and A0 of the Tx NodeMcu ESP 8266 board. The pins D3-D6 are pulled up by 4x10K resistors connected to +3.3V. These pins are designed in the code by GPIO 0, GPIO 2, GPIO 14 and GPIO 12 respectively. For the feedback acknowledgement we used the monochrome Oled 0.94" display (SSD1306) connected at +3.3V, GND, D1, (Oled SCK), and D2, (Oled SDA), pins, (Fig. 1.a, b).

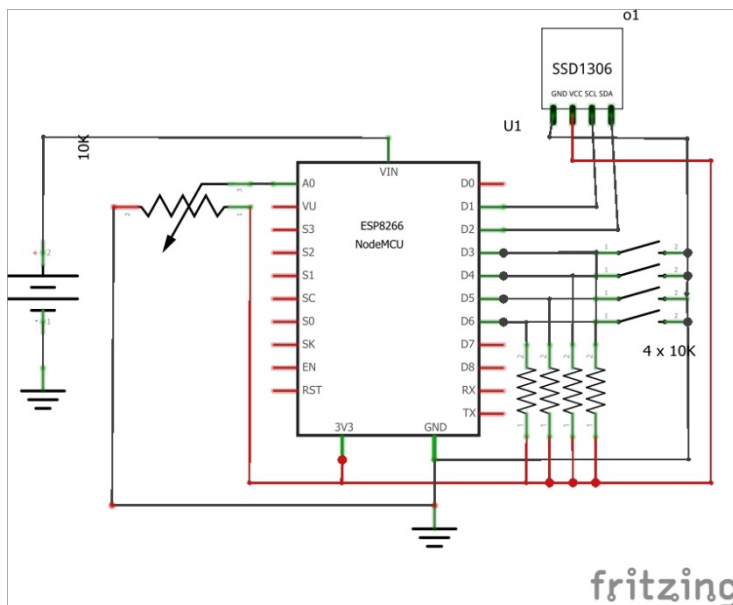


Fig. 1. a. The electric diagram of the Tx board

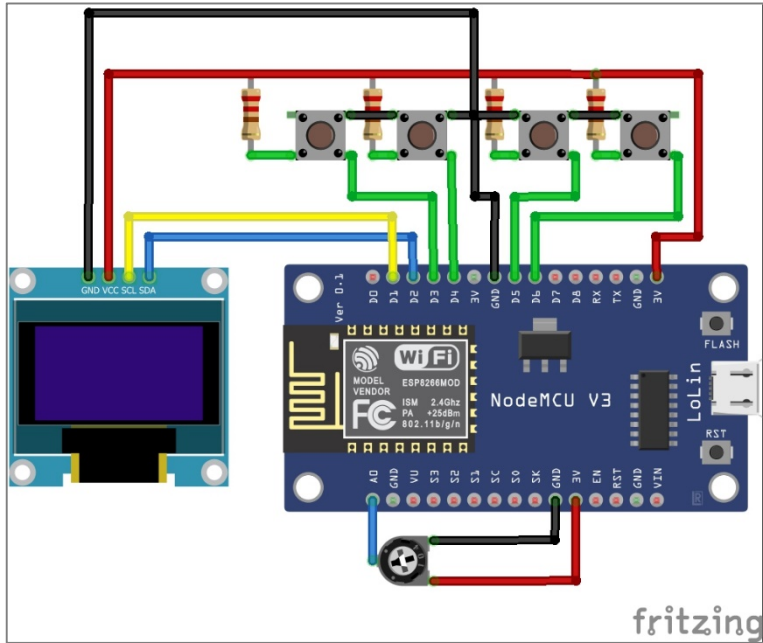


Fig. 1. b. The physical connection of the electric parts of the Tx board

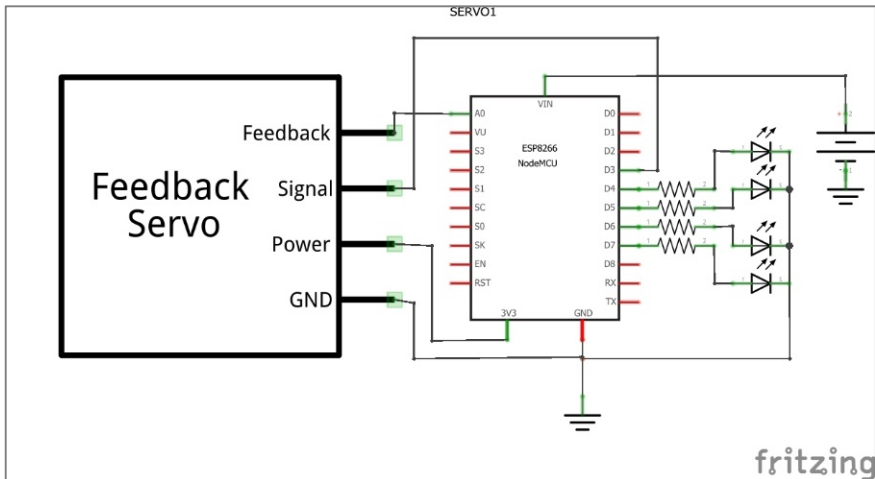


Fig. 2. a. The electric diagram of the receiver with feedback servo and 4 led.

The Rx contains 4 led connected to pins D5, D6, D7, D8, (designed by GPIO 14, GPIO 12, GPIO 13, GPIO 15 in the code), and GND and one servo connected to +3.3V, GND and D3, (GPIO 0 in the code), (Fig. 2 a). The wiper of the servo is connected to A0 pin for feedback. To access the wiper of the potentiometer we must open the servo and solder a wire as shown in figure 2. b, [4, 5]. Another version of the receiver contains two DC motors driven by the H bridge L 298 (or MX 1508) and the servo SG 90. The entries IN1-IN4 of the H bridge are connected to pins D5-D8, (Fig. 3 a, b). The codes for both versions of the receiver are the same. All parts of the system, the electronics and the motors are powered by a single 5V supply voltage connected between Vin and GND of NodeMcu board, but for high torque DC motors the bridge must be powered by a separately source, [6, 7].

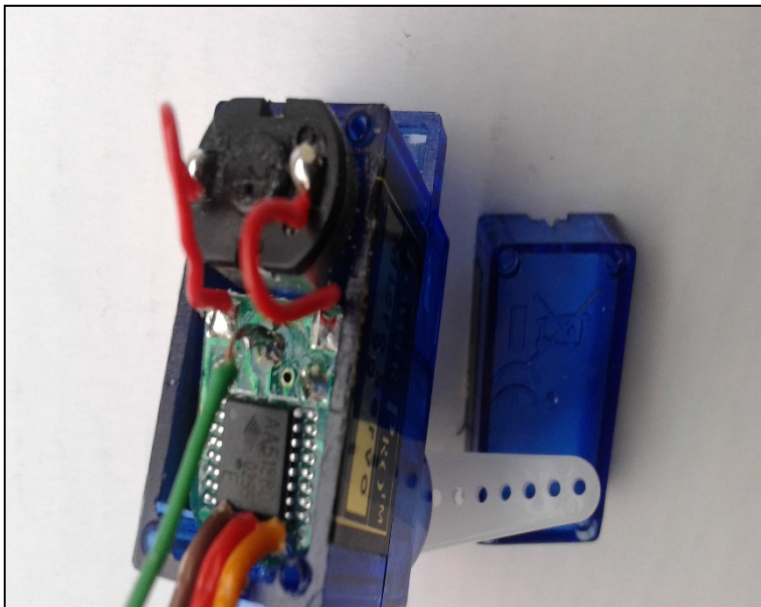


Fig. 2. b. Feedback connection of the servo SG 90. The green wire is connected to the wiper of the servo.

RESULTS AND DISCUSSION

The two-way communication between the ESP8266 NodeMCU boards is based on the use of the ESP-NOW protocol developed by Espressif, (ESP-NOW), [8]. This is a fast communication protocol that enables multiple devices to exchange small messages (up to 250 bytes) between them. It is very versatile, allowing one-way or two-way communication without using Wi-Fi. The main feature of this protocol is the possibility to establish connection between the desired device using their own MAC addresses. The use of this protocol with Arduino IDE implies some stages. First we need to set the Arduino IDE to recognize and communicate with the ESP 8266 board. Only the latest versions of Arduino, i.e. 1.8.13 version, have this facility. To do this we need to insert in the Arduino IDE > File> Preferences the following address: http://arduino.esp8266.com/stable/package_esp8266com_index.json.

Then on the Boards Manager we must install the “ESP8266 by Community” board, [9]. Then we must install the libraries requested by the code. The `espnnow.h` library comes installed by default when installing the ESP8266 board. The ESP-NOW protocol allows to define from the beginning the role of each device, “master” or “slave”, but also to change the role of devices from “master” to “slave” and vice versa. The first feature is used for the unilateral communication, when one device is set as transmitter and the other one as receiver, the role of each device remaining unchanged. The second feature is used for bilateral communications, when the transmitter sends the message to the receiver, after that it passes on the receiver mode, waiting the acknowledgement message from the receiver. The second device is set as receiver, but after receiving the message from the transmitter, it passes on the sender mode in order to transmit the acknowledgement message. After that the device returns to its initial state of receiver, waiting from a new message. To perform this operation each device must know the MAC address of its correspondent. In this way the connection is established only between desired devices, allowing other devices to use the same frequency channels. The MAC addresses can be obtained with a supplementary code presented below. The code must be uploaded to both devices. After running the code the MAC address is displayed on the Serial Monitor, [10]. When compiling the code, we must select the ESP8266 board in the Boards menu.

```
// The MAC addresses code:

#ifdef ESP32
#include <WiFi.h>
#else
#include <ESP8266WiFi.h>
#endif

void setup(){
  Serial.begin(115200);
  Serial.println();
  Serial.print("ESP Board MAC Address: ");
  Serial.println(WiFi.macAddress());
}

void loop(){
}
// end of the code
```

In the unilateral communication the MAC address of the receiver must be introduced only in the code of the sender. The role of each device, sender or receiver is established from the beginning by the code. For bilateral communication the MAC addresses are necessarily for both the partners of connection. The devices change the role, sender or receiver, in function of the code, for which reason each board need to know the other MAC address.

We present only the codes for bilateral communication.

```
// The sender code.

#define analogPin A0 //potentiometer connected to A0
#include <Wire.h>

#include <Adafruit_GFX.h>
#include <Adafruit_SSD1306.h>

#define SCREEN_WIDTH 128 // OLED display width, in pixels
#define SCREEN_HEIGHT 64 // OLED display height, in pixels
```

```

// Declaration for an SSD1306 display connected to I2C (SDA, SCL pins)

#define OLED_RESET -1 // Reset pin # (or -1 if sharing Arduino reset pin)
Adafruit_SSD1306 display (SCREEN_WIDTH, SCREEN_HEIGHT, &Wire, OLED_RESET);

#include <ESP8266WiFi.h>
#include <espnow.h>

// REPLACE WITH THE MAC Address of your receiver
uint8_t broadcastAddress[] = {0x84, 0x0D, 0x8E, 0xAA, 0xA3, 0xA3};

// Define the variables to be sent for each button
int temperatureX;
int temperatureY;
int temperatureZ;
int temperatureQ;
float analog;

// Define variables to store incoming readings
int incomingTempX;// led 1
int incomingTempY;// led 2
int incomingTempZ;// led 3
int incomingTempQ;// led 4

float incomingAn;//for servo

// Updates readings every 0.2 seconds initial,
const long interval = 200;
unsigned long previousMillis = 0; // will store last time button data were updated

// Variable to store if sending data was successful
String success;

//Structure example to send data
//Must match the receiver structure
typedef struct struct_message {
    int tempX;
    int tempY;

```

```

int tempZ;
int tempQ;
float ana;
} struct_message;

// Create a structure message called Readings to hold sensor readings
struct_message Readings;

// Callback when data is sent
void OnDataSent(uint8_t *mac_addr, uint8_t sendStatus) {
  Serial.print("Last Packet Send Status: ");
  if (sendStatus == 0){
    Serial.println("Delivery success");
  }
  else{
    Serial.println("Delivery fail");
  }
}

// Callback when data is received
void OnDataRecv(uint8_t * mac, uint8_t *incomingData, uint8_t len) {
  memcpy(&incomingReadings, incomingData, sizeof(incomingReadings));
  Serial.print("Bytes received: ");
  Serial.println(len);
  incomingTempX = incomingReadings.tempX;
  incomingTempY = incomingReadings.tempY;
  incomingTempZ = incomingReadings.tempZ;
  incomingTempQ = incomingReadings.tempQ;

  incomingAn = incomingReadings.ana;
  //for Servo
}

void getReadings(){

  temperatureX=digitalRead(12);
  //button on D6 defined in the code by GPIO 12
  temperatureY=digitalRead(14);

```

```

//button on D5 defined in the code by GPIO 14
temperatureZ=digitalRead(0);
//button on D3 defined in the code by GPIO 0
temperatureQ=digitalRead(2);
//button on D4 defined in the code by GPIO 2

analog = analogRead(analogPin);
//potentiometer for servo
}

void printIncomingReadings(){
//display on OLED
  display.clearDisplay();
  display.setTextSize(2);
  display.setCursor(0,0);
  display.print("An:");
  display.print(incomingAn);
  display.print(" ");

  display.setCursor(0, 25);
  display.print("Y:");
  display.print(incomingTempY);
//receive back from the Rx the data sent for led command
  display.print(" X:");
  display.print(incomingTempX);

  display.setCursor(0, 50);
  display.print("Z:");
  display.print(incomingTempZ);

  display.print(" Q:");
  display.print(incomingTempQ);
  display.setCursor(110, 56);
  display.display();
}

void setup() {
pinMode(14, INPUT);

```

```

pinMode(12, INPUT);
pinMode(0, INPUT);
pinMode(2, INPUT);
// buttons connected to D3, D4, D5, D6

if(!display.begin(SSD1306_SWITCHCAPVCC, 0x3C)) {
  Serial.println(F("SSD1306 allocation failed"));
  for(;;); // Don't proceed, loop forever
}
display.clearDisplay();
display.setTextColor(WHITE);

Serial.begin(115200);

// Set device as a Wi-Fi Station
WiFi.mode(WIFI_STA);
WiFi.disconnect();

// Init ESP-NOW
if (esp_now_init() != 0) {
  Serial.println("Error initializing ESP-NOW");
  return;
}

// Set ESP-NOW Role
esp_now_set_self_role(ESP_NOW_ROLE_COMBO);

// Once ESPNow is successfully initialized, we will register for Send CB to
// get the status of transmitted packet
esp_now_register_send_cb(OnDataSent);

// Register peer
esp_now_add_peer(broadcastAddress, ESP_NOW_ROLE_COMBO, 1, NULL, 0);

// Register for a callback function that will be called when data is received
esp_now_register_recv_cb(OnDataRecv);
}

```

```

void loop() {
  unsigned long currentMillis = millis();
  if (currentMillis - previousMillis >= interval) {
    previousMillis = currentMillis;

    //Get buttons readings
    getReadings();
    //Set values to send
    Readings.tempX = temperatureX;
    Readings.tempY = temperatureY;
    Readings.tempZ = temperatureZ;
    Readings.tempQ = temperatureQ;

    Readings.ana = analog;
    //read potentiometer
    // Send message via ESP-NOW
    esp_now_send(broadcastAddress, (uint8_t *) &Readings, sizeof(Readings));

    // Print incoming readings
    printIncomingReadings();
  }
}
// End of the code

```

The MAC address of the receiver is introduced into the code of the transmitter by the following line of the code:

```

// REPLACE WITH THE MAC Address of your receiver
" uint8_t broadcastAddress[] = {0x84, 0x0D, 0x8E, 0xAA, 0xA3, 0xA3}; "

```

The transmitter is set as sender by default, but after transmitting the order it passes in receiver mode and wait for the feedback message. The following line of the code is responsible for this job.

```

"esp_now_set_self_role(ESP_NOW_ROLE_COMBO);"

```

Other explanations are included into the code.

The corresponding receiver code is presented below:

```
// Receiver code

#include <Servo.h>
Servo Servo1;
int angle=80;
#define analogPin A0 //leg pot la A0

#include <Wire.h>

#include <ESP8266WiFi.h>
#include <espnow.h>

// REPLACE WITH THE MAC Address of the sender
uint8_t broadcastAddress[] = {0x84, 0x0D, 0x8E, 0xB0, 0xCE, 0x62};

int temperatureX;
int temperatureY;
int temperatureZ;
int temperatureQ;
// variables for led control
float analog;

// Define variables to store incoming readings
int incomingTempX;// led 1
int incomingTempY;// led 2
int incomingTempZ;// led 3
int incomingTempQ;// led 4
float incomingAn;

const long interval = 200;
unsigned long previousMillis = 0;
// Variable to store if sending data was successful
String success;

//Structure example to send data
//Must match the sender structure
typedef struct struct_message {
    int tempX;
```

```

int tempY;
int tempZ;
int tempQ;

float ana;
} struct_message;
struct_message Readings;

// Create a struct_message to hold incoming data
struct_message incomingReadings;

// Callback when data is sent
void OnDataSent(uint8_t *mac_addr, uint8_t sendStatus) {
  Serial.print("Last Packet Send Status: ");
  if (sendStatus == 0){
    Serial.println("Delivery success");
  }
  else{
    Serial.println("Delivery fail");
  }
}

// Callback when data is received
void OnDataRecv(uint8_t * mac, uint8_t *incomingData, uint8_t len) {
  memcpy(&incomingReadings, incomingData, sizeof(incomingReadings));
  Serial.print("Bytes received: ");
  Serial.println(len);
  incomingTempX = incomingReadings.tempX;
  incomingTempY = incomingReadings.tempY;
  incomingTempZ = incomingReadings.tempZ;
  incomingTempQ = incomingReadings.tempQ;

  incomingAn = incomingReadings.ana;
  //for servo
}

void getReadings(){

```

```

temperatureX=incomingTempX;
temperatureY=incomingTempY;
temperatureZ=incomingTempZ;
temperatureQ=incomingTempQ;
analog = analogRead(analogPin);
}
void setup() {
  pinMode(15, OUTPUT);
  pinMode(14, OUTPUT);
  pinMode(13, OUTPUT);
  pinMode(12, OUTPUT);

  digitalWrite(15, LOW);
  digitalWrite(14, LOW);
  digitalWrite(13, LOW);
  digitalWrite(12, LOW);

  Servo1.attach(0);//servo on D3

  Serial.begin(115200);

  // Set device as a Wi-Fi Station
  WiFi.mode(WIFI_STA);
  WiFi.disconnect();

  // Init ESP-NOW
  if (esp_now_init() != 0) {
    Serial.println("Error initializing ESP-NOW");
    return;
  }

  // Set ESP-NOW Role
  esp_now_set_self_role(ESP_NOW_ROLE_COMBO);

  // Once ESPNow is successfully Init, we will register for Send CB to
  // get the status of Trasnmitted packet
  esp_now_register_send_cb(OnDataSent);

```

```

// Register peer
esp_now_add_peer(broadcastAddress, ESP_NOW_ROLE_COMBO, 1, NULL, 0);

// Register for a callback function that will be called when data is received
esp_now_register_recv_cb(OnDataRecv);
}
void loop() {
  unsigned long currentMillis = millis();
  if (currentMillis - previousMillis >= interval) {
    previousMillis = currentMillis;
    getReadings();

    // Set values to send
    Readings.tempX = temperatureX;
    Readings.tempY = temperatureY;
    Readings.tempZ = temperatureZ;
    Readings.tempQ = temperatureQ;
    Readings.ana = analog;

    // Send message via ESP-NOW
    esp_now_send(broadcastAddress, (uint8_t *) &Readings, sizeof(Readings));

    if (incomingTempX == 1) {
      digitalWrite(14, LOW);
    }
    else {
      digitalWrite(14, HIGH);
    }

    if (incomingTempY == 1) {
      digitalWrite(15, LOW);
    }
    else {
      digitalWrite(15, HIGH);
    }

    if (incomingTempZ == 1) {
      digitalWrite(13, LOW);
    }
  }
}

```

```

}
else {
digitalWrite(13, HIGH);
}
if (incomingTempQ == 1) {
digitalWrite(12, LOW);
}
else {
digitalWrite(12, HIGH);
}

angle = map(incomingAn, 0, 1023, 0, 180);
//Map the readings values to an angle from 0 to 180
  Servo1.write(angle);
}
}
// End of the code

```

After receiving the data the receiver passes in sender mode, in order to ensure the feedback. The following line is responsible for this action:

```
<esp_now_set_self_role(ESP_NOW_ROLE_COMBO);>
```

The receivers read the state of the led and of the servo and send back these data to the sender for feedback.

```
<void getReadings(){...}>
```

After that it come back in the receiver mode and waits for new data.

Other explanations of how the code is working are included into the code itself. It works with both the circuits presented in figures 2 and 3. Every time when a button is pressed on the Tx board, the corresponding led on the Rx board, or the corresponding DC motor, pass in ON state and the OLED display change from 1 to zero. When the potentiometer is rotate on the Tx board, the servo attached to Rx board rotate with the corresponding angle, and the value of the real angle of rotation is send back to the Tx. This value is displayed on the OLED.

CONCLUSION

The work demonstrates the possibility to establish direct bilateral communication between two NodeMcu ESP8266 boards without the use of intermediate devices. The system is used to control servos, DC motors or led. During the transmission each board change the role from receiver to sender and vice versa, ensuring the duplex communication. This action is ordered by specific programming code installed into each device. The communication is established only between desired devices, identified by theirs own MAC addresses. The duplex communication allows the feedback action between the receiver and sender. Real time feedback is achieved by particularly connection of the servo to the NodeMcu ESP8266 board.

REFERENCES

1. M. Todica, Feedback control of DC motors with long range HC 12 Transceiver and Arduino, Studia Univ. "Babes-Bolyai", Physica, Vol. 64 (LXIV), 1-2, 2019, pp. 91-100
DOI:10.24193/subbphys.2019.10
2. M. Todica, Software feedback with HC 12 transceivers and Arduino Research Gate
DOI:10.13140/RG.2.2.24560.61444
3. Arduino Website ([www.arduino.cc/en/Guide/ Introduction](http://www.arduino.cc/en/Guide/Introduction))
4. M. Todica, Servo and RGB led feedback with smartphone and Blynk, Research Gate,
DOI:10.13140/RG.2.2.23512.08960
5. http://dr-iguana.com/prj_TPro_SG90_2/
6. T. A. Antal, Acta Technica Napocensis, Series: Applied Mathematics, Mechanics, and Engineering, Vol. 60, Issue I, March (2017)
7. S. D. Anghel, Bazele Electronicii analogice si digitale, Presa Universitară Clujeană, Cluj-Napoca, 2007, ISBN: 978-973-610-554-8
8. Rui Santos, Getting Started with ESP-NOW (ESP8266 NodeMCU with Arduino IDE), <https://randomnerdtutorials.com/esp-now-esp8266-nodemcu-arduino-ide/>
9. Rui Santos, Installing ESP8266 Board in Arduino IDE (Windows, Mac OS X, Linux), <https://randomnerdtutorials.com/how-to-install-esp8266-board-arduino-ide/>
10. Rui Santos, Get ESP32/ESP8266 MAC Address and Change It (Arduino IDE)
<https://randomnerdtutorials.com/get-change-esp32-esp8266-mac-address-arduino/>

RESISTANCE OF HIGH-TC SUPERCONDUCTORS: REVIEW ARTICLE

C. LUNG^{1,*}, D. MARCONI², M. POP³, A.V. POP¹

ABSTRACT. The origin of resistance and its relation to the superconducting mechanism remain a profound, unsolved mystery. Currently, model parameters used to fit normal state properties are specific and vary arbitrarily from one doping. This short review illustrates the electrical resistivity of ceramic high temperature superconductors copper oxides. The article gives a summary of the prevailing arguments of researchers to relate the material to ceramic HTS compounds.

Keywords: *superconductivity, HTC ceramic compounds, resistivity.*

INTRODUCTION

The discovery of superconductivity at 40 K by Bednorz and Muller and at 90 K by Wu and Chu, in the ceramic oxides, has generated a tremendous amount of work in the field of high temperature superconducting materials. Superconductors with high critical temperatures are extremely complex and it remains difficult to synthesize high quality samples. In this regard, the materials and crystallographic aspects, drawing together the fields of structural chemistry and physics, solid state chemistry and physics, and applications and properties, both for cuprate and organic superconductors, play a vital role in our understanding of the phenomenon. Since the realization of electrical conducting properties of HTC ceramic compounds, there have been extensive investigations in to their transport properties. The significant progress of ceramic materials has been attracted attention of a lot of scientists in various disciplines and encouraging their entry into field. The synergy of diverse scientific senses brings further spread of the study of these materials.

¹ Babeş-Bolyai University, Faculty of Physics, 1 Kogălniceanu Str., 400084 Cluj-Napoca, Romania.

² Department of Molecular and Biomolecular Physics, National Institute for Research and Development of Isotopic and Molecular Technologies, Cluj-Napoca, Romania.

³ Department of Materials Science and Engineering, Technical University Cluj-Napoca, Bvd. Muncii Street Romania.

* Corresponding author: claudiu.lung@phys.ubbcluj.ro

Electrical resistance of ceramic HTC compounds

Ceramic HTS compounds can be considered as grain systems coupled to each other by Josephson junctions. Some of these junctions behave as weak intergranular bonds (WJs) as shown in the literature. These lead to increased contact resistivity ρ_{ct} between the grains, and the electrical conduction is of the percolative type (mobile load carriers move on the roads where they meet the lowest values for ρ_{ct}). Because inside the grains we also have a percolative conduction along the CuO_2 layer (ab plane), the intragranular coupling between two crystallites will be in relation with the match between the CuO_2 layers at their boundary. When the CuO_2 planes make large angles between them or if they break at the contact limit of the granules ρ_{ct} grow.

For Bi: 2212 compounds with optimal gap doping in the CuO_2 layers (therefore maximum T_C) the electrical resistivity changes depending on the temperature as in Figure 1 [1].

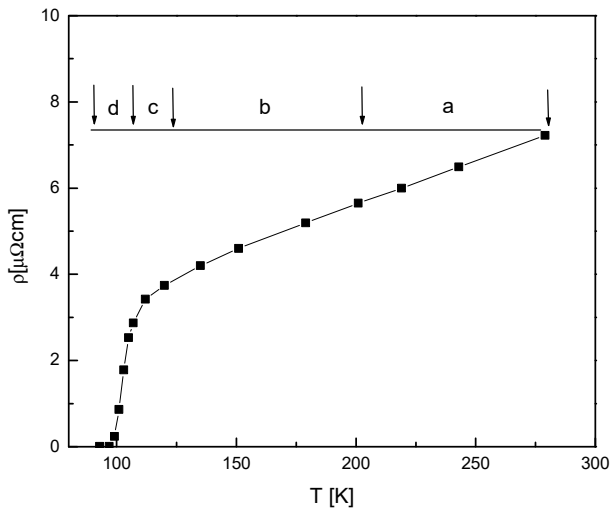


Fig. 1. Electrical resistivity as a function of temperature for the superconducting system Bi: 2212

We find the presence of four dependent regions $\rho(T)$: a) the "metallic" region; b) region of excess conductivity; c) the region of transition from the normal state to the superconducting state; d) the region of dissipative processes in the vortex system of the mixed state.

a) "Metallic" region

In this region the resistivity varies linearly depending on the temperature:

$$\rho = \rho(0) + aT$$

where $\rho(0)$ is the residual resistivity (obtained by extrapolating to $T=0K$ the linear dependence) and $a = \frac{d\rho}{dT}$ it is the slope of the right. This region is usually between temperatures $T^* \approx 2T_C$ and room temperature. Electrical conduction is called the "metallic" type because of the dependence $\rho(T)$ is formally described by a law similar to that encountered in metals: $\rho(T) = \rho(0) + \rho_{ph}(T)$, where $\rho_{ph}(T) = \alpha T$ is the phonon contribution in the limit of high temperatures, and $\rho(0)$ is the temperature-independent residual resistivity.

In the case of metals, $\rho(0)$ comes from the scattering of electrons on impurities or static imperfections of the network and $\rho_{ph}(T)$ from the scattering of electrons on the phonons of the network. Because the two scattering processes are not coherent, the scattering probabilities (which are proportional to the inverse of the relaxation times) add up:

$$\frac{1}{\tau} = \frac{1}{\tau_r} + \frac{1}{\tau_i} .$$

In this expression τ_r and τ_i are the relaxation times of the electrons following the scattering of photons in the network, respectively impurities. We notice that $\rho_{ph} \approx \frac{1}{\tau_r}$, and $\rho(0) \approx \frac{1}{\tau_i}$. Due to the inconsistency of the two scattering processes responsible for the resistivity of metals, there is no link between $\rho(0)$ and $\rho_{ph}(T)$ or $\alpha = \frac{d\rho_{ph}}{dT}$.

Compared to the situation presented above, we find major differences in HTS compounds. If in homogeneous metals the conduction is three-dimensional (3D), in HTS compounds the behavior of "metal" type is generally found for the two-dimensional conduction (2D) in the CuO_2 layers. Another difference is given by the fact that between the slope $\alpha_{ab} = \frac{d\rho_{ab}}{dT}$ (describing the linear dependence of the resistivity in the plane (ab) as a function of temperature: $\rho_{ab}(T) = \rho_{ab}(0) + \alpha_{ab}T$

and value ρ_{ab} measured at 100K there is a linear correlation [2]. This was highlighted in a set of 5 single crystals of $\text{YBa}_2\text{Cu}_3\text{O}_7$ with the same value for the critical temperature, $T_c = 91\text{K}$, but different values for α_i and $\rho_{ab}(100)$. The explanation of this behavior can be given based on the model of percolative conduction in single crystals. This model considers that:

$$\rho_{ab}(T) = p(\rho_i(0) + \alpha_i T)$$

At the ideal crystal, without defects, it is expected as $\rho_i(0) \rightarrow 0$, and $p \rightarrow 1$. Changing the slope of the linear dependency, $\alpha_{ab} = p\alpha_i$, is therefore directly related to the current percolation parameter. The defects in the plane (ab) caused by the disorder of the oxygen atoms, the small angles between the planes (ab), respectively their twinning, change the value of p.

In the case of HTS ceramics, dependence $\rho(T)$ can be written as:

$$\rho(T) = p[\rho_{ab}^i(T) + \rho_{ct}]$$

where $\rho_{ab}^i(T)$ is the intrinsic resistivity of the single crystal ($\rho_{ab}^i(T) = \rho_i(0) + \alpha_i T$) and ρ_{ct} is the contact resistivity between the granules.

In the case of polycrystalline ceramics, it was considered that the dependence of resistivity as a function of temperature is mainly determined by $\rho_{ab}(T)$, because resistivity ρ_c after the direction c is a few orders of magnitude larger than in the plane (ab) [3]. Resistivity ρ_{ct} independent of temperature is the average resistivity due to structural inhomogeneities of much larger dimensions than the size of the distances characteristic of the system (coherence length, average free path, distance between atomic layers, etc.). Such inhomogeneities occur at the contact of two grains or two untouched domains. For easier interpretation of percolative processes, p is used instead $\frac{1}{q}$. The low values of q suggest a sharp decrease in the cross section through which the electric current can pass due to the porosity of the sample and the decrease in the length of the percolation path between the granules due to the random orientation of the planes (ab) at the junction of neighboring granules. For these reasons the resistivity increases strongly. When the planes (ab) in the neighboring granules make small angles between them and engage well, then $q \rightarrow 1$. In general, the values of q are between zero and the unit $0 < q < 1$. important ρ_{ct} and p (or $\frac{1}{q}$) that characterize the

ceramic samples can be estimated based on the determination from the experimental data of the values $\rho(0)$ and $a = \frac{d\rho}{dT}$ intrinsic $\alpha_i = \frac{d\rho_{ab}}{dT} \cong 0,5\mu\Omega\text{cmK}^{-1}$ and $\rho_i(0)$ of the monocrystalline sample.

b) Excess of conductivity region

This region begins at $T^* = 2T_C$ where the deviation from the linear metallic type dependence appears and ends at the CT. To characterize this area, the experimentally measured resistivity ρ_m is compared, with the one extrapolated from the linear temperature dependence of ρ . At the temperature $T < T^*$ we observe that $\rho_m < \rho$, so the measured conductivity $\sigma_m = \frac{1}{\rho_m}$ is greater than $\sigma = \frac{1}{\rho}$ [1]. The difference $\Delta\sigma = \sigma_m - \sigma > 0$ it is called excess conductivity. This phenomenon was first demonstrated experimentally by Glover in measurements of electrical resistivity in amorphous bismuth thin films [4].

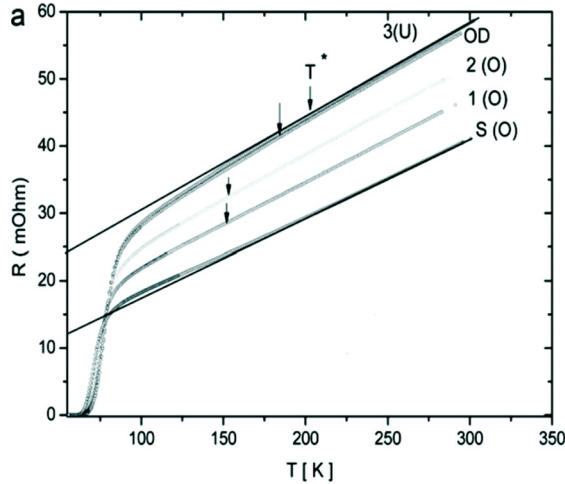


Fig. 2. The in-plane resistance R vs. temperatures T for overdoped states of Bi-2212 with $x = 0.02$ Zn

D. Marconi et al. shows that the temperature dependence of in-plane electrical resistance $R = R_{ab}$, of epitaxial Bi-2212 film with $x = 0.02$ Zn, in different doping states obtained after removing oxygen from in situ state S (O). Critical

transition temperature T_c obtained from the maximum of first derivative dR/dT data shows that OD is the optimal doped state (with maximum value of T_c), states S (O), 1 (O), 2 (O) are small overdoped states, and state 3 (U) is a small underdoped state (very close to OD). The resistance increases steadily with decreasing oxygen content. The typical high T-linear behavior followed by a less rapid decrease of $R(T)$ at lower temperatures and a slight upward curvature of $R(T)$ in the overdoped state S (O), can be seen in Figure 2. [23].

c) The transition region from the normal state to the superconducting state

This region is characterized by a sudden decrease in resistivity as the temperature decreases. The critical temperature T_C is considered in the position of the inflection point of the curve $\rho(T)$ through the transition zone where the numerical derivative $\frac{d\rho}{dT}$ is canceled. An evaluation of the T_C value can be done by the "midpoint" method. This method approximates with a straight line the curve AB $\rho(T)$ from the transition area (Figure 3).

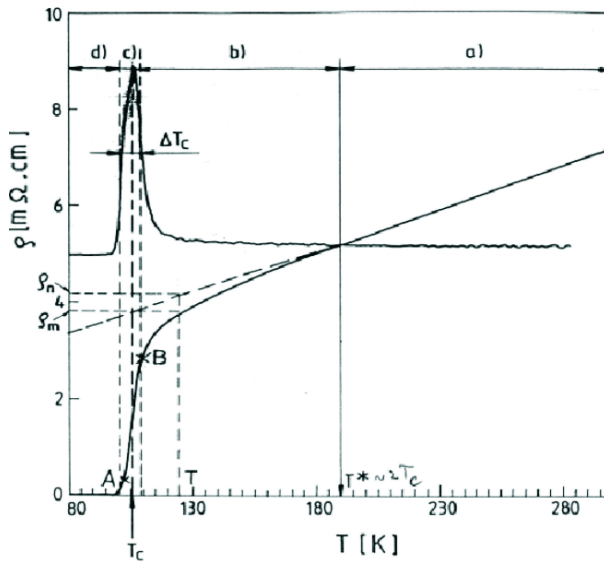


Fig. 3. Electrical resistivity as a function of temperature for (Bi, Pb): 2223 superconducting system [1].

A and B points are usually in the positions defined by the values 10% ρ_0 and 90% ρ_0 . The width of the transition is defined in this case as straight $(T_A - T_B) = \Delta T_C$, and the critical temperature T_C is in the middle of this range: $T_C = T_B + \frac{\Delta T_C}{2}$. The exact value of the transition width is given by the width ΔT of the peak of the numerical derivative $\frac{d\rho}{dT}$ measured at half its height [1].

d) Broadening of superconducting transition

As an example of the widening of the resistive transition in the magnetic field we will show in Fig.4 data from Palstra et al. [5-8] for $\text{Bi}_2\text{Sr}_2\text{CaCu}_2\text{O}_{8+\delta}$ configuration ($j \perp c, B \parallel c$). It is observed that by increasing the magnetic field there is a decrease in temperature for which the resistance is zero T_{c0} , and the width of the transition increases.

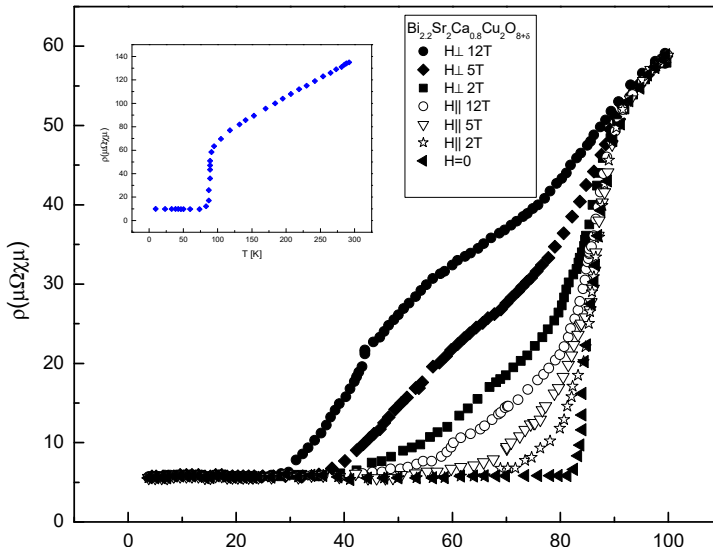


Fig. 4. Temperature resistivity for different magnetic field values. The applied magnetic field is: parallel to the c -axis (symbols open on the graph) or perpendicular to the c -axis (symbols closed on the graph)

Broadening the transition $\Delta T_c(B) = T_c(0) - T_c(B)$ In the presence of the magnetic field strongly depends on the value of the ratio ρ/ρ_n (ρ_n represents the temperature-dependent resistivity of the normal state). Transition width $\frac{\Delta T_c}{T_c} = 1 - \frac{T}{T_c}$, varies nonlinearly with the magnetic field according to a law of the type:

$$1 - T/T_c \sim B^\nu$$

exponent ν varies in different studies, however it is often close to $2/3$ [9, 10-12]. This behavior is the result of the shape of the irreversibility line and shows that the width of the resistive transition and the appearance of the irreversibility line are related. Results similar to those in Fig. 4 have been found for crystals, epitaxial films and polycrystals from all major HTSC families. To $\text{La}_{2-x}\text{Sr}_x\text{CuO}_4$; $\text{YBa}_2\text{Cu}_3\text{O}_{7-\delta}$; [13,12,14,1] systems based on Bi [15-17,1,18-20] and Tl [21,22].

e) Thermally activated resistivity

The bottom of the resistive transition ($\rho/\rho_n \approx 10^{-6} - 10^{-2}$) was studied in detail by Palstra et al. They found the thermally activated resistivity [5,7,8] to be of the form:

$$\rho = \rho_0 \exp \left[- \frac{U}{k_B T} \right] \quad (1)$$

then the characteristics IV become linear for both configurations (j c, B c) and (j c, B || c). We present the results for $\text{Bi}_2\text{Sr}_2\text{CaCu}_2\text{O}_{8+\delta}$ (B || c) in Fig.5 in the representation of Arrhenius $\ln \rho$ depending on $1/T$. The slope in this representation is interpreted as the activation energy U. It is of the order of 103K for $\text{Bi}_2\text{Sr}_2\text{CaCu}_2\text{O}_{8+\delta}$ [18-20] and decreases with increasing magnetic field. factor ρ_0 it is found to be a few orders of magnitude larger than the resistivity of the normal state. Similar results were reported for Tl-coated superconductors and for the 60K phase of $\text{YBa}_2\text{Cu}_3\text{O}_{7-\delta}$ [7].

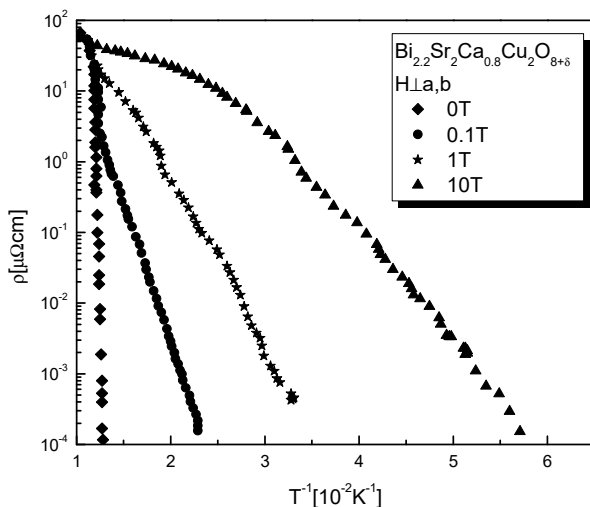


Fig. 5. Representation of Arhenius for the data in Figure 4 in the case of the superconductor $Bi_2Sr_2CaCu_2O_{8+\delta}$ and $B \parallel c$

SUMMARY

In conclusion, in the presented material were discussed some experimental results obtained for electrical resistance of ceramic HTC compounds. We show and detailed the presence of four temperature dependent regions of electrical resistivity: a) the "metallic" region; b) region of excess conductivity; c) the region of transition from the normal state to the superconducting state; d) the region of dissipative processes in the vortex system of the mixed state.

REFERENCES

1. G. Ilonca, A. V. Pop, *Supraconductibilitatea și supraconductorii cu temperaturi critice înalte*, ed. BIT Iași, (1998).
2. A.V. Pop, G.H. Ilonca, D. Ciurchea, V. Pop, A. Konopko, I.I. Geru, M. Todica, V. Ioncu, *Int. J. Mod. Phys. B* 9 (1995) 695.
3. S. J. Hagan, *Phys. Rev. B* 37, 7928 (1998).
4. R.E. Glover, *Phys. Lett.* 25 A, 542 (1997).
5. T.T.M. Palstra, B. Batlogg, L.F.Schneemeyer, and J.V. Waszczak, *Phys. Rev. Lett.* 61, 1662 (1988).

6. T.T.M. Palstra, B. Batlogg, R.B. van Dover, L.F. Schneemeyer, and J.V. Wanzczak, *Appl. Phys. Lett.* 54, 763 (1989).
7. T.T.M. Palstra, B. Batlogg, R.B. van Dover, L.F. Schneemeyer, and J. V. Wanzczak, *Phys. Rev.* B41, 6621 (1990).
8. B. Batlogg, T.T.M. Palstra, L.F. Schneemeyer, and J.V. Wanzczak, p 368 in *Strong Correlation and Superconductivity*, H. Fukuyama, S. Maekawa, A.P. Malozernoff (eds.), Springer Series in Solid-State Sciences, Vol. 89 (1989).
9. M. Tinkham, *Phys. Rev. Lett.* 61, 1658 (1988).
10. B. Oh, K. Char, A.D. Kent, M. Naito, M.R. Beasley, T H. Geballe, R.H. Hammond, and A. Kapitulnik, *Phys. Rev.* B37, 7861 (1988).
11. P. Mandal, A. Poddar, A.N. Das, B. Ghosh, and P. Choudhury, *Physica C*169, 43 (1990).
12. K. Kitazawa, S. Kambe, and M. Naito, p. 361, *Strong Correlation and Superconductivity*, H. Fukuyama, S. Maekawa, A.P. Malozernoff (eds.), Springer Series in Solid-State Sciences, Vol. 89 (1989).
13. K. Kitazawa, S. Kambe, M. Naito, I. Tanaka, and H. Kojima, *Jap. J. Appl. Phys.* 28, L555 (1989).
14. S. Kambe, TN. Naito, K. Kitazawa, Tanaka, and H. Kojima, *Physica C*160, 243 (1989).
15. N. Kobayashi, H. Iwasaki, H. Kawabe, K. Watanabe, H. Yamane, H. Kurosawa, H. Masumiote, T. Hirai, and Y. Moto, *Physica C*159, 295 (1989).
16. J.Y. Juang, J.A. Cutro, D.A. Rudman, R.B. van Dover, L.F. Schneemeyer, and J.V. Wanzczak, *Phys. Rev.* B38, 7045 (1988).
17. R.B. van Dover, L.F. Schneemeyer, E.M. Gyorgy, and J.N. Wanzczak, *Phys. Rev.* B39, 4800 (1989).
18. G. Ilonca, A.V. Pop, D. Benea, C. Lung, M. Ilonca and R. Deltour *Modern Phys. Lett. B*, vol. 12, No.25, 1081-1088 (1998).
19. G. Ilonca, A.V. Pop, T. Jurcut, C. Lung and R. Deltour *Physica C*, 284 -288, 1097 - 1098 (2000).
20. G. Ilonca, A. V. Pop, G. Stiufiuc, R. Stiufiuc and C. Lung, *Modern Physics Letters B*, Vol. 15, No. 22, 1141 - 1046 (2001).
21. J.H. Kang, K.E. Gray, R.T. Kampwirth, and D.W. Day, *Appl. Phys. Lett.* 53, 2560 (1988).
22. H. Iwasaki, N. Kobayashi, N1. Kikuchi, T. Kajitani, Y. Syono, Y. Muto, and S. Nakajima, *Physica C*159, 301 (1989).
23. D. Marconi, M. Pop, *J. Alloys Comp.* 513, 586 - 591 (2012).